TU Wien

Master Thesis

Electrochemical Switching Behaviour of Exsolution Catalysts

Author:
Melanie Maurer

Supervisors:
Projektass. Dipl.-Ing.
Harald Summerer

Projektass.(FWF) Dipl.-Ing.
Christoph Riedl

Assistant Prof. Dipl.-Ing.
Dr.techn.
Alexander Opitz

Univ. Prof. Dr. rer. nat.
Jürgen Fleig

A thesis submitted in fulfilment of the requirements for the degree of Master of Science at the

Institute of Chemical Technologies and Analytics

Melanie Maurer

Monat Jahr, Vienna

Hauptstrasse 149 , 2122 Münichsthal

Abstract

Recently, catalyst preparation through exsolution of catalytically active metal species from perovskite-type host oxides have gained significant interest. This type of catalyst offers various attractive advantages such as a high degree of dispersion, a very low tendency to agglomerate since they are anchored in the host oxide, and the possibility of reactivation by redox cycling after the poisoning event. Beyond that, it was shown that exsolution catalysts offer the interesting feature of being electrochemically switchable between a very active metallic state and a less active oxidic state. This is of particular interest for heterogeneous catalysis, as it allows controlling the oxidation state of the catalyst particles on the surface of an electrode, irrespective of the equivalent $p(O_2)$ of the surrounding atmosphere. However, the interplay between electrode, atmosphere and particle is still insufficiently understood. Therefore, a better understanding of the electrochemical switching behaviour, particularly of the exsolved catalyst particles is of significant interest. In this thesis, the electrochemical triggered exsolution of metallic particles and the resulting switching behaviour between high and low activity states was investigated on different perovskite-type electrode materials. These measurements were

carried out on model-type $La_{0.6}Sr_{0.4}FeO_{3-\delta}$ (LSF) and $Nd_{0.6}Ca_{0.4}FeO_{3-\delta}$ (NCF) thin film electrodes, which were grown by pulsed laser deposition on single crystalline yttria-stabilized zirconia (YSZ) electrolyte. In the first step, the exsolution of Fe particles was triggered upon applying cathodic polarisation and the resulting effect on the electrochemical behaviour was studied via impedance (AC) and direct current (DC) measurements. In addition, also the effect of time and atmosphere composition (H_2:H_2O ratio in Ar) on the exsolution onset was systematically studied. Next, on electrodes successfully decorated with exsolved particles, the impact of the effective $p(O_2)$ in the atmosphere on the electrochemical switching behaviour was investigated and the relevance of the applied overpotential and the oxygen partial pressure on the switching reaction was analysed. Further experiments were conducted to see how doping with elements easier reducible than iron (e.g. B-site doping with 10 % Co) influences the initial exsolution behaviour as well as the electrochemical switchability of the studied exsolution catalysts. The gained results identified fractionated exsolution in multi-B-site-cation containing perovskites as an interesting future topic, e.g. investigating a broader range of dopants (Ni, Cu) and their potential application in heterogeneous catalysis.

Kurzfassung

In letzter Zeit hat die Katalysatorherstellung durch Exsolution katalytisch aktiver Metallspezies aus Kristallgittern vom Perowskit-Typ stark an Interesse gewonnen. Diese Art von Katalysatoren bietet verschiedene Vorteile wie einen hohen Dispersionsgrad, eine sehr geringe Tendenz zur Agglomeration, da sie an der Oberfläche des Materials verankert sind, und die Möglichkeit der Reaktivierung durch Redoxzyklen nach einem Vergiftungsereignis. Darüber hinaus wurde gezeigt, dass Exsolutionskatalysatoren die viel versprechende Eigenschaft haben, elektrochemisch zwischen einem sehr aktiven metallischen Zustand und einem weniger aktiven oxidischen Zustand umschaltbar zu sein. Dies ist für die heterogene Katalyse von besonderem Interesse, da es erlaubt, den Oxidationszustand der Katalysatorpartikel auf der Oberfläche einer Elektrode zu steuern, unabhängig vom äquivalenten $p(O_2)$ der umgebenden Atmosphäre. Wie dieses Wechselspiel zwischen Elektrode, Atmosphäre und Partikel im Detail abläuft, ist jedoch noch unzureichend erforscht. Daher ist ein besseres Verständnis des elektrochemischen Schaltverhaltens der exsolvierten Katalysatorpartikel von großem Interesse. In dieser Arbeit wurde die elektrochemisch ausgelöste Exsolution von metallischen Partikeln

und das daraus resultierende Schaltverhalten zwischen hohen und niedrigen Aktivitätszuständen an verschiedenen Elektrodenmaterialien vom Perowskit-Typ untersucht. Diese Messungen wurden an den Modelltypen $La_{0.6}Sr_{0.4}FeO_{3-\delta}$ (LSF) und $Nd_{0.6}Ca_{0.4}FeO_{3-\delta}$ (NCF) Dünnschichtelektroden, die durch gepulste Laserabscheidung auf einkristallinem Yttriumoxid-stabilisiertem Zirkoniumdioxid (YSZ) Elektrolyt gewachsen sind. Im ersten Schritt wurde das Exsolutionverhalten der Fe-Partikel durch Anlegen einer kathodischen Polarisation untersucht und der daraus resultierende Effekt auf das elektrochemische Verhalten mittels Impedanz- (AC) und Gleichstrommessungen (DC) gemessen. Darüber hinaus wurde auch der Einfluss von Zeit und Atmosphärenzusammensetzung (H_2:H_2O-Verhältnis in Ar) auf den Beginn der Exsolution systematisch untersucht. Außerdem wurde an Elektroden, an denen sich bereits Partikel an der Oberfläche befinden , der Einfluss des effektiven $p(O_2)$ in der Atmosphäre auf das elektrochemische Schaltverhalten untersucht und die Relevanz der angelegten Überspannung und des Sauerstoffpartialdrucks auf die Schaltreaktion analysiert. In zusätzlichen Experimenten wurde untersucht, wie die Dotierung mit Elementen, die leichter reduzierbar sind als Eisen (z.B. B-Site-Dotierung mit 10 % Co) das anfängliche Exsolutionsverhalten sowie die elektrochemische Schaltbarkeit der untersuchten Exsolutionskatalysatoren beeinflusst. Durch die erzielten Ergebnisse konnte die fraktionierte Exsolution in Multi-B-Site-Kationen enthaltenden Perowskiten erzielt werden, was ein interessantes Zukunftsthema darstellt, z.B. die Untersuchung eines breiteren Spektrums von Dotierstoffen (Ni, Cu) und deren potentielle Anwendung in der heterogenen Katalyse.

Acknowledgement

This adventurous and eventful year in which I was able to conduct and write my master's thesis has taught me a lot, including how important it is to show gratitude to all those who have helped me get this far. Therefore, I want to thank Univ. Prof. Jürgen Fleig for giving me the opportunity to be a part of his research group and providing a well equipped laboratory. Moreover, I want to sincerely thank Alexander Opitz who always stood by my side with advice and support.

A very big thank you to my two super kind and helpful supervisors Harald Summerer and Christoph Riedl. They were always very patient and supportive, even when I lost the fourth sample in the microscope. I also thank Harald Summerer for making his measurement setup available to me, especially for introducing me to Python and providing his scripts. Without him I would probably still be debugging. In addition, his LaTeX preamble saved me from my first grey hairs, which Word would undoubtedly have given me.

My gratitude also goes to everyone in the research group for making the time I spent here fun, varied and creating an enjoyable working environment, despite the prevailing pandemic. A particular thank you to Alex Schmied, for explaining many Python intricacies to me, as well as Christin Böhme, who was a massive help with all Mac-specific problems and for making my time in the office very pleasant. A special thank you to my good friend and colleague Kristen Rath. I can not tell you how often she stood with me over the last few months, whether at the university or in my private life. Whether we were despairing together, climbing or cooking, she was always a great friend.

I also want to thank my other colleagues who I could hardly see due to the problematic situation, but who have always accompanied me over the last few years. A massive thank you to Irina Wodak, with whom I locked myself in the stairwell on my first day at university. Without her, I would never have made it through the first year.

Finally, I would also like to thank all my other friends and my family who always gave me tissues and wine when university drove me to crazy. A big thank you to my boyfriend Liam, who stood with me through the pandemic and my last Master's year. Without him, it would have been much harder and, above all, boring.

Contents

1 Introduction

Climate change has a strong effect, not only on individual countries but the entire globe. The European Union (EU) has committed itself through the European climate legislation to become climate neutral by 2050 [1]. In order to limit global warming to 1.5 °C, it is necessary to ensure climate neutrality by the middle of the 21^{st} century. Climate neutrality is achieved when the amount of carbon dioxide emitted to the atmosphere equals the amount of CO_2 removed from the atmosphere by carbon sinks. Estimations show that natural sinks remove between 9.5 and 11 Gt of CO_2 per year [2]. However, in 2019, annual global CO_2 emissions were 36 Gt [3], which were almost 4 times the amount of the naturally removed CO_2. Due to these circumstances dramatical changes are necessary to accomplish the set goal of climate neutrality. In December 2019 the EU presented the ”Green Deal” in order to accomplish the Paris Agreement, which also refers to the energy sector and its amount of emitted CO_2 [4]. One way to reduce CO_2 emissions is to use energy more efficiently. Hence, energy conversion with fuel cells may play an important role in the future, as they offer a significantly higher level of efficiency compared to conventional power generation technologies.

Currently, a very large part of the energy required is produced by heat engines, based on the principle of the Carnot process. This way of energy provision requires several conversion steps from one form of energy into anther one, which results in a significant amount of energy getting lost due to these various conversion steps. In comparison to this conventional production of electrical energy, solid oxide fuel cells (SOFC) offer many advantages and are therefore an opportunity to overcome several challenges of efficient energy conversion. Fuel cells allow the direct transformation of fuel into electrical energy, thus bypassing the detour via thermal or mechanical energy and thus avoiding energy loss. Therefore, SOFCs have a significantly higher theoretical efficiency. The achieved conversion efficiency of SOFCs is up to 60 % electrical and a wide range of fuels can be used [5]. A sketch of a SOFC is shown in Fig. 1.1. Like in case of any other electrochemical cell, the working principle relies on the separation of oxidation and reduction half reaction by an electrolyte. In case of a SOFC, the electrolyte conducts oxide ions, while the electrons have to travel from one electrode to the other via the external circuit.

In general SOFCs consist of an electrolyte, a porous anode and a porous cathode. As electrolytes zirconium based materials are commonly used, which exhibit a satisfying ionic conductivity at high temperatures (600 - 1000 °C) [6]. Molecular oxygen is reduced to O^{2-} at the cathode and incorporated into the electrode. After passing the cathode electrolyte interface the oxygen ions subsequently migrate through the electrolyte to the anode, where hydrogen is oxidised to water [7]. While there are multiple types of fuel cells, so called proton exchange membrane fuel cells (PEMFCs) are currently state of the art [8–11]. This, however, limits its

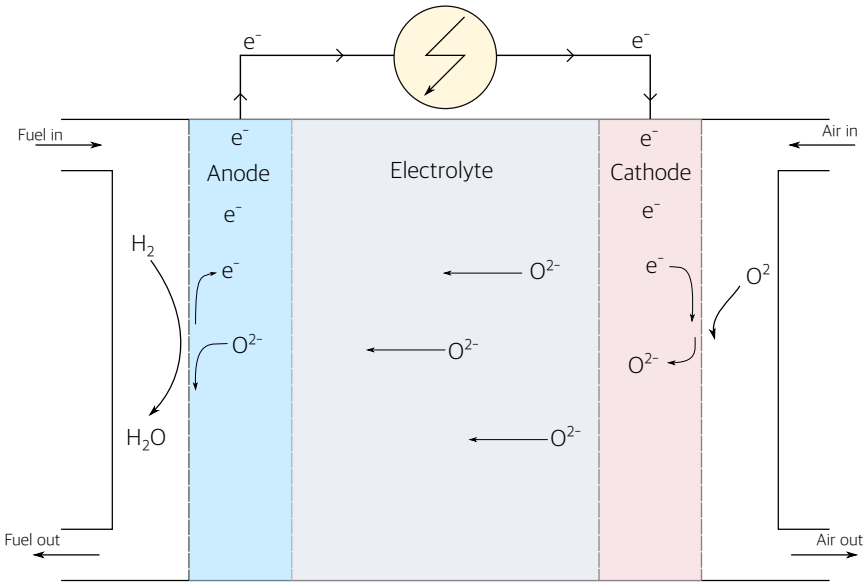

Figure 1.1: Schematic sketch of a SOFC

operating temperature and therefore its kinetics. In contrast to SOFCs, the mobile ions in PEMFCs are protons, thus water is formed at the cathode. The higher operating temperatures of SOFCs result not only in faster kinetics but also allow a broader range of fuels (CO, syngas, biogas,etc.), since especially CO as an intermediate product in case of any carbon based fuel does not poison the anode by its strong adsorption behaviour as this is the case in PEMFCs. Therefore, SOFCs are an attractive alternative for industrial application [12, 13].

Not only energy efficiency, but also the usage of renewable energy plays an import role in recent years. Unfortunately energy supplies such as sun or wind energy have only irregular availability (both through the course of a day or throughout sn entire year) and thus energy storage is essential in an energy scenario fully based

on renewables. Hydrogen, for example, is expected to play a major role for energy storage. By using solid oxide electrolysis cells (SOECs), water can easily be turned into hydrogen, which can then be stored and converted back via SOFCs [14, 15] .

The most frequently used material for SOFC anodes is a composite material consisting of metallic Ni and the electrolyte material YSZ [16]. Unfortunately, one major disadvantage of Ni/YSZ is the thermomechanical instability under oxidising conditions at high temperature, where Ni easily oxidises to NiO and loses its catalytic potential. [17] Even though ceramic-metallic (cermet) anodes have good properties using H_2 as fuel, they are very sensitive to sulfur [18] and clogging (the formation of carbon fibres when using carbon containing gas), which results in strong performance losses [19]. To overcome these problems, anodes based on electronically conducting ceramics can be used instead of Ni/YSZ [20].

As a certain drawback, the catalytic activity of mixed ionic/electronic conductors (MIECs) for hydrogen oxidation lags somewhat behind that of cermets. To circumvent this problem, the surface of the oxide can be tuned through decoration with catalytically active (nano)particles [21], thus introducing catalytic activity without the disadvantage of redox-induced mechanical stresses. However, the simple deposition of metallic particles onto an oxide surface produces particles, which are prone to agglomeration over time [22]. The growth of metallic nano-particles from a perovskite-type oxide, which initially contains the respective metal in its lattice, is a method capable of producing particles partly embedded into the host oxide and thus anchored on its surface. This approach was firstly demonstrated by Nishihata and co-workers for Pd doped La(Fe,Co)O_3 [23]. In their work the authors showed

that while Pd was incorporated into the host lattice of a La(Fe, Co)O_3 perovskite under oxidising conditions, at reducing conditions Pd nanoparticles formed on the sample surface. In addition, switching back to oxidising conditions under relatively high temperatures (900 °C) lead to reincorporation of the particles into the perovskite. The authors called these catalysts ”intelligent catalysts” due to their selferegenerating ability based of the exsolving/redissolving depending on the surrounding atmosphere. Nowadays, this phase separation producing particles on the surface of an oxide upon a reductive treatment is commonly referred to as exsolution [24–27].

Various studies have shown that there is also a huge potential for exsolution catalysts in SOFC anodes and thus it is necessary to get a better knowledge of the physical and catalytical behaviour of these materials [28–31]. One very interesting ability of exsolution catalyst is their electrochemical switchablilty, when using the perovskite-type MIEC host oxide as electrode on an ion conducting electrolyte. This allows to control the effective p_{O_2} in the mixed conducting electrode and the application of a cathodic overpotential can thus trigger the exsolution of metallic particles at the surface [32–34]. Vice versa, applying an anodic polarisation can re-oxidise the particles [34]. If this is done at moderate temperatures, the mobility of cations in the oxide is too small for an immediate redissolution of the oxidised particles in the host oxide and hence changing the applied voltage between cathodic and anodic, causes switching of the oxidation state of the particles [35]. Since the catalytic properties of the metallic and the oxidic particles are strongly different, the electrochemical switching between oxidation states goes hand in hand with a

switching of the catalytic activity of the exsolutions. For H_2 electro-oxidation on $La_{0.6}Sr_{0.4}FeO_{3-\delta}$ (LSF) electrodes carrying Fe exsolutions, for example, a reversibility between the active Fe^0 and the inactive Fe-oxide (Fe_3O_4,FeO) could be observed at 625 °C. As a result, a change in the slope of the voltage-current characteristic was observed, acting as an indicator for the electro-catalytic activity of the exsolved Fe particles [35].

The main goal of this thesis is to investigate the electrochemical switching behaviour of different perovskite-type electrodes. In particular, the role of applied cathodic voltage and polarisation time on the initial exsolution as well as the effects of the effective $p(O_2)$ in the atmosphere on the electrochemical switching point (i.e. the transition between metallic and oxidic particles) shall be investigated. Therefore, different working electrodes were prepared from the scratch and analysed via electrochemical impedance spectroscopy (EIS) and voltage-current curves. First $La_{0.6}Sr_{0.4}FeO_{3-\delta}$ and $Nd_{0.6}Ca_{0.4}FeO_{3-\delta}$ were investigated via different DC measurements by varying the parameters of the reaction conditions. Later on, A- and B-sited doped perovskites ($Nd_{0.6}Ca_{0.4}Fe_{0.9}Co_{0.1}O_{3-\delta}$) was studied to get first insight into exsolution and electrochemical switching behaviour of perovskites containing two exsolvable species in the same host lattice.

2 Theoretical Background

2.1 Crystal Structure and Defects in Solids

In principle, solids can be divided in amorphous and crystalline materials. In contrary to amorphous solids, crystalline solids possess long-range order and 3-dimensional translation symmetry. In general, a crystal consists of a lattice (translational symmetry) and a basis (point group), which is defined by the type, number, and arrangement of atoms inside the unit cell, which is the smallest repetitive part of the structure and has the form of a parallelepiped. The complete symmetry of a crystal is included in the unit cell. A combination of the point group and the translational symmetry leads to space group symmetry. The lengths and the angles between the edges of the unit cell are described by the lattice parameters. There are seven different lattice systems, which differ in the length of the lattice vectors and geometric arrangement of the three lattice vectors. Taking into account different centering of the lattices (primitive, face-centred, body-centred, base-centred) 14 different lattices symmetry types (Bravais lattices) are obtained. Moreover, there are 32 crystallographic point groups and 230 space groups [36].

In solid state electrochemistry, defects have a major impact on electronic and/or ionic conductivity. A perfect crystal without any defects does not exist as it is energetically unfavoured. Defects decrease the Gibb's free energy in the system, as the formation of defects cause an increase of the entropy [37].

In general defects are classified by their dimension [38] :

- **0-Dimensional defects** : point defects
  - Occur around a single lattice point
  - Can be further subdivided into **intrinsic** and **extrinsic** defects
- **1-Dimensional defects** : linear defects
  - Dislocations
- **2-Dimensional defects** : plane defects
  - Affecting external and internal surfaces and interfaces e.g. grain boundaries
- **3-Dimensional defects** : volume defects
  - Point defect clusters or precipitates, pores

In the further chapters point defects will be described in more detail, due to their ability to induce ionic and electronic conductivity in materials such as perovskites (ABO_3), which play an important role throughout this thesis.

2.2 Point Defects

As already mentioned, point defects can be divided into intrinsic and extrinsic defects. An intrinsic defect is formed by a crystal itself, whereas extrinsic defects, as the name implies, are caused by external factors such as impurities or doping. These defects have an important impact on chemical and physical properties and therefore influence the electrochemical behaviour of ionic solids. In order to systematise and standardise the notation of point defects and thus make it possible to write down chemical reactions involving point defects, Kröger and Vink suggested the notation shown in Eq. (2.1) [39]:

$$M_S^C \tag{2.1}$$

M in Eq. (2.1) denotes a certain species e.g. atoms/ions, vacancies (v), electron holes (h) or free electrons (e). S corresponds to the lattice site, which is occupied by species M. It usually corresponds to the symbol of the occupant in a perfect crystal or an i in the case of interstitials. C denotes the electronic charge of M relative to the site it occupies. The charge can either be neutral (x), positive ($^\bullet$) or negative ($'$).

2.2.1 Intrinsic Defects

Since defects are thermodynamically favoured as they lead to an increase in entropy, crystalline systems tend to naturally include them. There a two common types of disorders in ionic crystals, which are shown in Fig. 2.1.

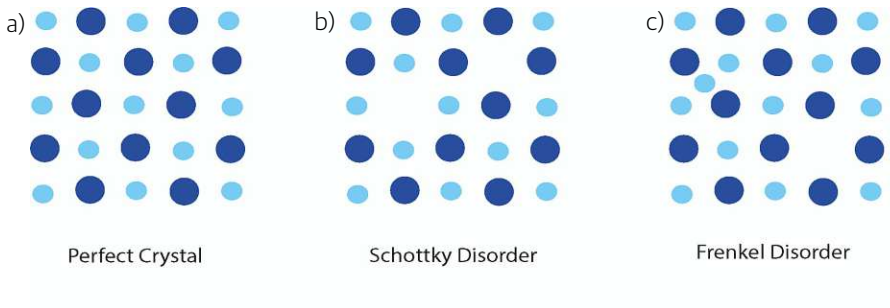

Figure 2.1: Schematic of a) a perfect crystal b) a Frenkel disorder and c) a Schottky disorder

In case of **Frenkel disorder** an atom moves to an interstitial site, where no atom usually appears. Moreover, one can differentiate between Frenkel and anti-Frenkel disorder, whereas the former refers to cations and latter to anions. Contrary, in a **Schottky disorder** cation vacancies and anion vacancies are generated in the ratio in which they occur in the unit cell. In both of these disorder types charge neutrality is preserved.

2.2.2 Extrinsic Defects

Extrinsic defects are classified according to their cause. On the one hand, if they are undesired and/or added by accident they are called impurities. On the other hand, if they are desired and added on purpose to improve the properties of the material, they are categorized as dopants. Mostly, when it comes to doped ceramics the amount of intrinsic defects is negligible in relation to the extrinsic defect concentration.

A distinction is made between two different types of dopants:

in terms of their charge relative to the ideal lattice

- **Donor dopants** possess a positive charge relative to the lattice site occupied, which can be for example an added cation being higher in valence than the host lattice ions. Therefore, to guarantee charge neutrality either cation vacancies, anion interstitials , or n-type electronic point defects are formed by the ionic lattice as a response to donor doping.

- **Acceptor dopants** possess a negative charge relative to the lattice site occupied e.g. if added cations are lower in valence than the host lattice ions. In order to balance this charge cation interstitials, anion vacancies or p-type electronic point defects (electron holes) are formed.

In ceramic SOFC electrodes and electrolyte materials doping is a common way to increase ionic and/or electronic conductivity. For example, in yttria-stabilized zirconia (YSZ) ZrO_2 is acceptor doped by adding Y_2O_3 (8 %). Y^{3+} occupies the lattice

site of Zr^{4+}, hence Y^{3+} is relatively negatively charged. In order to compensate the initial charge, oxygen vacancies are formed. This presence of vacant sites in the oxygen sublattice allows oxygen ions to move through the lattice and thus ionic conductivity is created. This reaction is shown in formula Eq. (2.2) in Kröger-Vink notation.

$$Y_2O_3 \xrightarrow{ZrO_2} 2\,Y'_{Zr} + V^{\bullet\bullet}_{O} + \frac{1}{2}\,O_2 \tag{2.2}$$

2.2.3 Non-Stoichiometric Defects

Another important source for point defects is the occurrence of non-stoichiometry, which is caused by a reaction of the crystal with the surrounding atmosphere. At a sufficiently high temperature an oxide will equilibrate with the surrounding atmosphere and O_2 will (depending on the oxygen partial pressure) be incorporated or released from the crystal (see Eq. (2.3)).

Oxygen incorporation and release

$$\frac{1}{2}\,O_2 + V^{\bullet\bullet}_{O} + 2\,e' \rightleftharpoons O^{\times}_{O} \tag{2.3}$$

As a consequence, the concentration of point defects in a solid vary with the oxygen partial pressure. If the defect model of a certain model is known, it is possible to calculate the oxygen partial pressure dependence of each point defect at a

certain temperature and summarize them in the so called Brouwer diagram. In the following, this is exemplary shown for $La_{0.6}Sr_{0.4}FeO_{3-\delta}$ (LSF) based on bulk data taken from Kuhn et al [40]. In LSF the A-site is doped with Sr^{2+}, which is relative to La^{3+} negatively charged (Sr'_{La}). Both elements have a fixed valence. However, Fe can change its valence and thus compensate the resulting charge in balance. In general, Fe^{3+} occupies the B-site of the lattice, in this state it is considered neutral ($Fe^{\times}_{Fe}$). If Fe is present as Fe^{2+} then it has a relatively negative charge (Fe'_{Fe}). However, if Fe is present as Fe^{4+} then it has a relatively positive charge ($Fe^{\bullet}_{Fe}$). Both Fe'_{Fe} and $Fe^{\bullet}_{Fe}$ can also be interpreted as n-type (e') and p-type ($h^{\bullet}$) electronic point defects localised on the B-site cation of LSF respectively. Moreover Sr, which occupies the A-site, can be compensated by inducing oxygen vaccines shown in Eq. (2.4).

$$Sr'_{La} \longrightarrow \frac{1}{2} V^{\bullet\bullet}_{O} \tag{2.4}$$

LSF can undergo oxygen exchange reactions, so oxygen can be released and incorporated in the material, this is shown in Eq. (2.5).

$$V^{\bullet\bullet}_{O} + \frac{1}{2} O_2 + 2\,Fe^{\times}_{Fe} \rightleftharpoons O^{\times}_{O} + 2\,Fe^{\bullet}_{Fe} \tag{2.5}$$

Taken this equilibrium in consideration it can be assumed that the defect concentrations relays on the surrounding oxygen partial pressure. In Eq. (2.6) the mass action law for an oxygen release reaction is shown.

$$K_{ox} = \frac{[O_O^x][\mathrm{Fe}_{\mathrm{Fe}}^{\bullet}]^2}{[\mathrm{V}_{\mathrm{O}}^{\bullet\bullet}][\mathrm{Fe}_{\mathrm{Fe}}^{\times}]^2\sqrt{pO_2}} \tag{2.6}$$

The amount of oxygen lattice sites in the crystal ([O]) can be described as sum of occupied lattice sites and oxygen vacancies with Eq. (2.7) and this can be used to eliminate one variable of Eq. (2.6).

$$[\mathrm{O}] = [\mathrm{V}_{\mathrm{O}}^{\bullet\bullet}] + [\mathrm{O}_{\mathrm{O}}^{\times}] \tag{2.7}$$

The disproportional of Fe^{3+} in the lattice leads to the equilibrium constant (K_i) in Eq. (2.8).

$$K_i = \frac{[\mathrm{Fe}_{\mathrm{Fe}}^{\bullet}][\mathrm{Fe}_{\mathrm{Fe}}^{\prime}]}{[Fe_{Fe}^{x}]} \tag{2.8}$$

As both electrons and electrons holes are located on the Fe they can be add to the amount of Fe^{3+} and this sum leads to the total lattice sites of Fe [Fe]), shown in Eq. (2.9), using this relation a variable of Eq. (2.8) can easily be eliminate, too.

$$[\mathrm{Fe}] = \mathrm{Fe}_{\mathrm{Fe}}^{\times} + \mathrm{Fe}_{\mathrm{Fe}}^{\prime} + \mathrm{Fe}_{\mathrm{Fe}}^{\bullet} = \mathrm{Fe}^{3+} + \mathrm{Fe}^{2+} + \mathrm{Fe}_4 \equiv \tag{2.9}$$

In order to keep the material neutral the following equilibrium, shown in Eq. (2.10) needs to be fulfilled.

$$[\mathrm{Sr}_{\mathrm{La}}^{\prime}] + [\mathrm{Fe}_{\mathrm{Fe}}^{\prime}] = 2\,[\mathrm{V}_{\mathrm{O}}^{\bullet\bullet}] + [\mathrm{Fe}_{\mathrm{Fe}}^{\bullet}] \tag{2.10}$$

To calculate the concentrations of oxygen vacancies, electron holes and electrons as a function of the oxygen partial pressure Eq. (2.6), Eq. (2.8) and Eq. (2.10) need to be combined. In order to determine K_i and K_{Ox} the thermodynamic data ($\Delta H_{Ox} = -95.62\,\mathrm{kJ\,mol^{-1}}$, $\Delta S_{Ox} = -54.27\,\mathrm{J\,mol^{-1}\,K^{-1}}$, $\Delta H_i = 95.75\,\mathrm{kJ\,mol^{-1}}$ and $\Delta S_i = -21.63\,\mathrm{J\,mol^{-1}\,K^{-1}}$ [40]) can be used and filled in Eq. (2.11) and Eq. (2.12). After cacculting K_i and K_{ox} there three unknows and there equations left, which makes the system of equations easily solvable.

$$K_{ox} = e^{-\frac{\Delta H_{ox}}{RT} + \frac{\Delta S_{ox}}{R}} \tag{2.11}$$

$$K_i = e^{-\frac{\Delta H_i}{RT} + \frac{\Delta S_i}{R}} \tag{2.12}$$

Fig. 2.2 shows the resulting Brouwer diagram of LSF at 600 °C for all relevant charge carriers, namely $V^{\bullet\bullet}$, $h^{\bullet}$, e'.

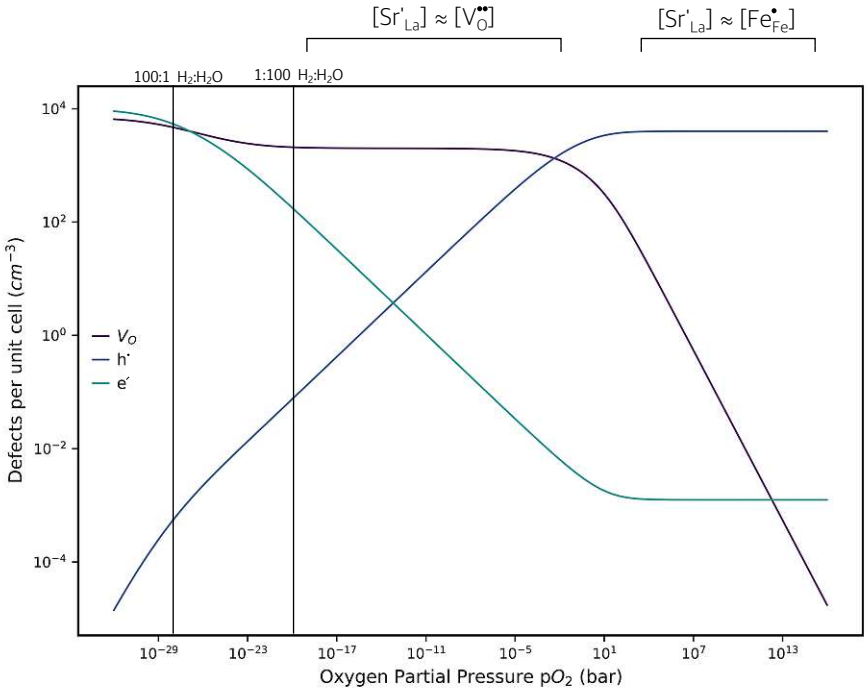

Figure 2.2: Schematic of a Brouwer diagram of LSF at 600 °C

The part of main interest for the experiments in this thesis was between 1×10^{-28} bar and 1×10^{-20} bar.

2.3 Mass and Charge Transport

When oxides contain oxygen vacancies, ionic oxygen is able to pass the crystal lattice by hopping from an occupied to a vacant oxygen site. Since oxide ions carry two negative charges not only mass but also charge is transported by this process through the lattice, resulting in a current. The driving force for diffusion of a species within a homogenous phase is defined as the gradient $\Delta\mu_i$ of the chemical potential μ_i within this phase. The concentration dependence of μ_i is given in Eq. (2.13).

$$\mu_i = \mu_0 + k_B T ln(x_i) \tag{2.13}$$

There in μ_0 denotes the chemical potential under standard conditions, x_i is the mole fraction, T is the temperature and k_B the Boltzmann constant. For $\Delta\mu_i = 0$ uncharged particles of species i are at equilibrium. For being able to describe also the transport of charged particles it is necessary to introduce the electrochemical potential $\tilde{\mu}_i$. In order to deduce the electrochemical potential from the chemical potential, the electial energy of the particle i needs to be taken into account. The electrical energy is given by the product of the charge number z_i of the particle, the elementary charge e and the electrical potential ϕ as shown in Eq. (2.14).

$$\tilde{\mu}_i = \mu_i + z_i e \phi \tag{2.14}$$

When the chemical equilibrium is reached, i.e. $\Delta\mu_i = 0$, the potential difference $\Delta\phi$ is the only driving force for a transport of particle i.

The electrochemical equilibrium is reached when $\Delta\tilde{\mu}_i = 0$. If there is a deviation from this equilibrium, a particle flux J_i will occur, which is described in Eq. (2.15) [41]

$$J_i = -\frac{\sigma_i}{z_i^2 e^2}\Delta\tilde{\mu}_i \tag{2.15}$$

In this equation, σ_i is the conductivity of species i within the considered phase. The conductivity depends on the concentration c_i and mobility u_i of the charged particle, as given by Eq. (2.16) .

$$\sigma_i = |z_i| e u_i c_i \tag{2.16}$$

In consideration of a mixed conducting material σ_{tot} describes the conductivity as the sum of the partial conductivities as shown in Eq. (2.17).

$$\sigma_{tot} = \sum_i \sigma_i = \sigma_{anions} + \sigma_{cations} + \sigma_{electrons} + \sigma_{holes} \tag{2.17}$$

2.4 Perovskites

In general, the structure of a perovskite is given by ABX_3, where A and B are cations and X is an anion. However, in the following X was subituted by O, because of the relvance of ABO_3 throughout this thesis. The crystal structure of a perovskite requires a larger cation on the A-site and a smaller cation on the B-site, which are coordinated by 12 and 6 O-anions, respectively. The lattice of a perovskite is shown Fig. 2.3, either with the A (left) or B (right) cation in center of the unit cell.

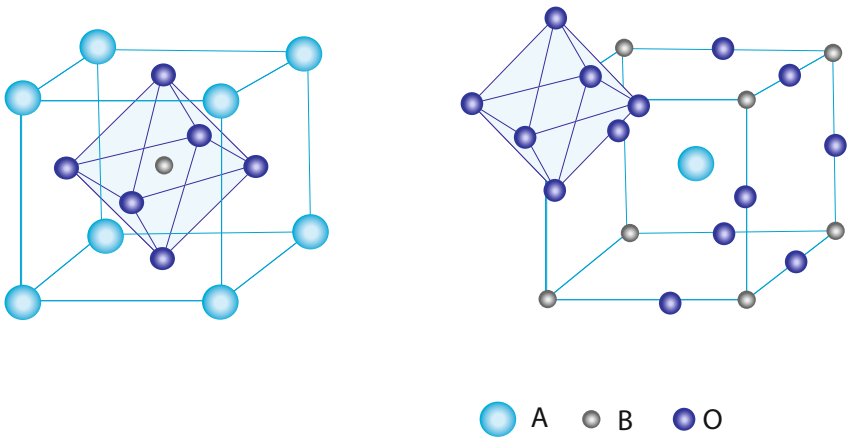

Figure 2.3: Schematic image of the crystal lattice of a cubic perovskite (ABO_3), with either A - or B as central atom

Considering the ideal cubic symmetry, which perovskites indeed are able to possess under certain conditions, the A cations form a cubic closed packed lattice. The B cations are located on the sites octahedral by coordinated by the oxygen ions. For different reasons the BO_6 octahedron can be distorted. A very common reason for

distortions in the perovskite lattice is a Goldschmidt tolerance factor significantly differing from one. The Goldschmidt tolerance factor t depends on the radius r of the ions A,B and O in the perovskite lattice shown in Eq. (2.18) [42].

$$t = \frac{r_A r_O}{\sqrt{2}(r_B + r_O)} \tag{2.18}$$

Another reason for distorted BO_6 octahedra in a perovskite is an elevated temperature. In such cases the perovskite has a rhombohedral, tetragonal or orthorhombic structure.

Moreover, perovskites can easily be doped and different cations can occupy the same lattice site thus forming a solid solution. In addition, the material strongly reacts to different oxygen partial pressures, which makes many perovskite-type materials are very interesting for different applications [37, 43]. This versatility makes them, for example, an interesting alternative for conventional electrode materials for SOFCs. Due to their tolerance of being doped by various elements their a very attractive option as host lattice for exsolution catalyst.

2.4.1 Exsolution

Perovskites are able to host certain catalysts as cations on the B site under oxidizing conditions. When bringing the material to strongly reducing conditions a partial exsolution of the hosted catalyst is possible, which leads to fixed nanoparti-

cles on the surface of the perovskite. However, exsolution can only be performed under strongly reducing conditions, which limits its application area. In order to overcome this challenge, a reducing overpotential can be applied. This cathodic bias makes it possible to perform exsolution in more oxidising conditions, which is very beneficial for their application. When it exsolution was performed the B-site cation partly exsolve out of the crystal lattice and remains on the surface as fixed nanoparticle. These fixed particles have the ability of electrochemical switching, which means they can be activated and inactived by an anodic bias. To monitor this behaviour I-V curves can be used, in which the electrochemical switching point can be observed as a discontinuity, due to the change in activity of the sample's surface [34, 35, 44]. In case of LSF exsolution can be induced either by the surrounding atmosphere and/or by applying a reductive overpotential, that can compensate for more oxidising atmospheres, shown in Eq. (2.19), Eq. (2.20), Eq. (2.21) and Eq. (2.22). In Fig. 2.4 a sketch of the used samples in this thesis and the described reactions are shown.

$$FeO + H_2 \rightleftharpoons Fe + H_2O \tag{2.19}$$

$$Fe_3O_4 + H_2 \rightleftharpoons 3\,FeO + H_2O \tag{2.20}$$

$$FeO + 2\,e^- \rightleftharpoons Fe + O^{2-} \tag{2.21}$$

$$Fe_3O_4 + 2\,e^- \rightleftharpoons 3\,FeO + O^{2-} \tag{2.22}$$

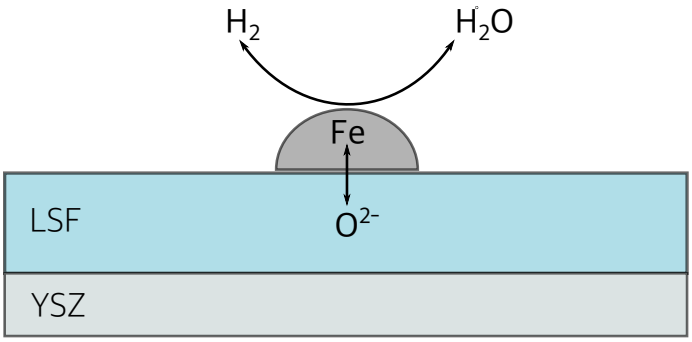

Figure 2.4: The change between catalytic Fe^0 and Fe-oxide on LSF induced either via H_2 or O^{2-}

In comparison to traditional deposition methods, exsolutions lead to better distributed particles and are more time- and cost-effective. Another advantage is the reversibility of the process, which means agglomeration can be avoided through reoxidation of the catalyst. It is proven that exsolution can be performed in both A-site-deficient and stoichiometric perovskites [45].

2.5 Measurement Techniques

2.5.1 Electrochemical Impedance Spectroscopy (EIS)

This electrochemical analysis method is a very common and simple and yet a powerful and non-destructive tool, even though the interpretation of the spectra can be quite difficult. As its name already implies, this technique is based on the frequency dependent measurement of the complex alternating current (AC) resistance, the impedance. During EIS measurements the respective samples and reactions on their electrode are in equilibrium, thus no net voltage is created.

To express the impedance in a formula, a ratio of voltage to current is used, as shown in Eq. (2.23). For EIS measurements a small sinusoidal voltage ($u(t)$) is applied to the electrochemical cell and the responding current ($i(t)$) is measured. For a linear response of the sample and thus a resulting harmonic sinusoidal current the impedance Z can be obtained as written in Eq. (2.23). $\hat{U}$ and $\hat{I}$ denote the amplitudes of u(t) and i(t), respectively, and ω describes the angular frequency. The amplitude ratio can also be denoted as Z_0.

$$\frac{u(t)}{i(t)} = \frac{\hat{U}sin(\omega t)}{\hat{I}sin(\omega t + \phi)} = Z_0 \frac{sin(\omega t)}{sin(\omega t + \phi)} \tag{2.23}$$

Eq. (2.23) can be transferred to the complex number range leading to Eq. (2.25). By using the Euler's relationship Eq. (2.24), ($j = \sqrt{-1}$). Due to that Z possess a real and imaginary part.

$$e^{j\phi} = cos(\phi) + jsin(\phi) \tag{2.24}$$

$$Z = Z_0 e^{j\phi} = Z_{Re} + jZ_{Im} \tag{2.25}$$

Depending on the behaviour of a sample, the contributions of Z_{Re} and Z_{Im} to the total impedance can be different. A resistor, for example, does not lead to a phase shift between potential and current, thus it has no imaginary part and can be described with Eq. (2.26), where R denotes the frequency independent resistance. In electrochemistry, long-range faradaic ionic or electronic charge transport appears as a resistor in impedance measurements. In contrast to a resistor, the AC current shifts by -90° when passing through a capacitor. Therefore, a capacitor consist solely of an imaginary part and can be described by Eq. (2.27), where C denotes the capacitance. This behaviour can appear either due to classical electrostatic displacement polarisation (either within a homogenous phase or at a phase boundary) or due to defect chemical changes within a phase (then called pseudo or chemical capacitance). To take possible non-ideal behaviour of a real system into account

the constant phase element (CPE) is introduced. In Eq. (2.28) the impedance of a constant phase element is described, where n and Q are parameters accenting for the non ideality. Parameter n ranges from 0 to 1 with the special case of n = 1 resulting in Q=C. The capacitance of a constant phase element can be obtained by Eq. (2.29) for the assumption of a normal distribution of characteristic frequencies [46].

$$Z_R = R \tag{2.26}$$

$$Z_C = \frac{1}{i\omega C} \tag{2.27}$$

$$Z_{CPE} = \frac{1}{(j\omega)^P T} \tag{2.28}$$

$$C_{CPE} = (R^{1-n}Q)^{\frac{1}{n}} \tag{2.29}$$

In EIS a very commonly appearing behaviour can be described as a parallel circuit of a resistor and a capacitor also called R||C element. As with DC measurements, Kirchhoff's laws apply to describe this network, resulting in Eq. (2.30).

$$Z_{R||C} = (\frac{1}{(Z_R)} + \frac{1}{Z_C})^{-1} = \frac{R}{1 + i\omega C} \tag{2.30}$$

The representation of impedance data can be done in various ways. Throughout this thesis the representation of data in the complex impedance (commonly called Nyquist plot) was used. In this diagram, the negative imaginary part of the impedance (Z_{IM}) (y-axis) is plotted versus the real part (Z_{RE}) (x-axis). In order to interpret impedance spectra a equivalent circuit (EC) is required. Through a complex non-linear least square fit, important parameters like resistances or capacitances can be obtained. In Fig. 2.5 however, in order to enable a physically meaningful interpretation of the parameters obtained, knowledge of the mechanistically correct equivalent circuit is necessary. A lack of detailed knowledge of the mechanism or non ideal behaviour that can only be insufficiently described with the available circuit elements are therefore often be the limitation of the method. One possible feature indicating non-ideal behaviour is the appearance of depressed semicircles. If such a depression is symmetrical, a R||CPE element can be used to treat this in data parametrisation. An exemplary comparison between ideal and depressed semicircle of R||C and R||CPE is shown in Fig. 2.5 [47].

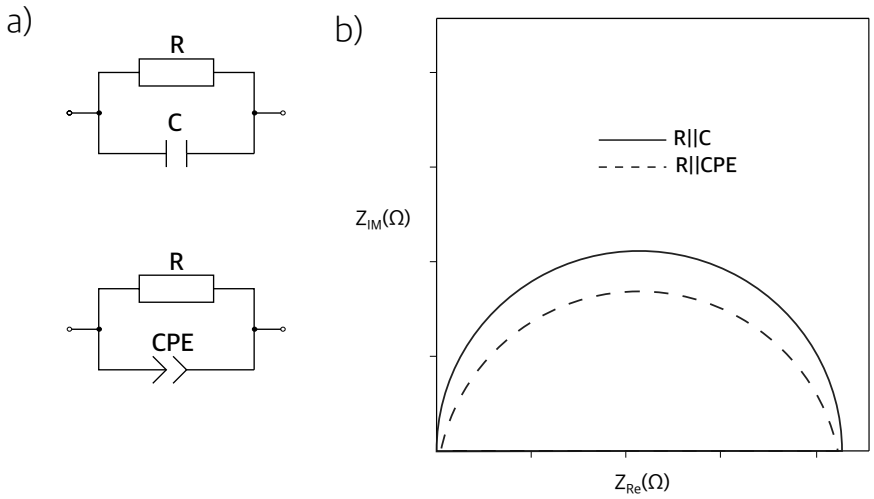

Figure 2.5: a) A model Nyquist plot showing the resistance of a capacitance CPE element and capacitor C, via its diameter b) equivalent circuits (EC) of an ideal R||C and a R||CPE element

2.5.2 Measurements with DC Bias

In contrast to impedance measurements, current-voltage measurements require the application of a DC current. As a consequence, the electrochemical cell is no longer in equilibrium and a net current results. According to Faraday's Law Eq. (2.31) this net current I is directly proportional to the moles of reactant n converted of the cell's electrode, and z the number by charges transferred in the cell reaction.

$$I = \frac{n}{t} zF \tag{2.31}$$

The applied DC bias brings the equilibrium of the corresponding reaction to one side, depending on its value. In the oxygen exchange reaction several species are involved and thus need to be considered, starting with the electrochemical potential of neutral oxygen ($\tilde{\mu}_O$), which is determined by the electrochemical potentials of electrons ($\tilde{\mu}_{e^-}$) and oxygen ions ($\tilde{\mu}_{O^{2-}}$) as shown in Eq. (2.32). A perfect counter electrode is continuously in equilibrium with the gas phase.

$$\tilde{\mu}_O = \tilde{\mu}_{O^{2-}} - 2\tilde{\mu}_{e^-} \tag{2.32}$$

The applied voltage between the working (WE) and counter electrode (CE) causes a difference in the electrochemical potentials of the electrons, described by Eq. (2.33), where F denotes the Faraday constant and U_{DC} describes, the applied voltage, i.e. bias.

$$\Delta\tilde{\mu}_{e^-} = -FU_{DC} \tag{2.33}$$

Due to the high electronic conductivity of the (MIEC) electrodes, the electrical potential is assumed to be constant within each electrode. The potential difference and the finite ionic conductivity of the electrolyte cause a change of the electrochemical potential of O^{2-} within the electrolyte. This change of $\Delta\mu_{O^{2-}}$ is shown in Eq. (2.34), where I_{DC} stands for the DC current and R_{YSZ} describes the ionic trans-

port resistance of the electrolyte.

$$\Delta\tilde{\mu}_{O_{2-}} = 2FI_{DC}R_{YSZ} \tag{2.34}$$

The voltage loss across the electrolyte is referred to the ohmic overpotential, see Eq. (2.35)

$$\eta_{YSZ} = I_{DC}R_{YSZ} \tag{2.35}$$

The electrochemical potential of the oxygen in the working electrode is defined by the electrochemical potentials of oxygen ions and electrons. The difference in the electrochemical potential of O_2 is because of the difference in the electrochemical potential of O^{2-} and e^-, shown in Eq. (2.36).

$$\Delta\tilde{\mu_O} = \Delta\tilde{\mu}_{O^{2-}} - 2\Delta\tilde{\mu_{e^-}} \tag{2.36}$$

In order to obtain the overpotential of the working electrode (η_{WE}) the applied bias (U_{DC}) needs to subtracted by the voltage drop caused by the electrolyte (η_{YSZ}), shown in Eq. (2.37). Therefore the η_{WE} can be seen as the fraction of the applied bias that is able to reach the working electrode.

$$\eta_{WE} = U_{DC} - I_{DC}R_{YSZ} \tag{2.37}$$

The different electrochemical potential of each species and their transfer from working to counter electrode, (considering an ideal system with porous counter electrode, i.e. a very fast counter electrode in an ideal cell) is shown in Fig. 2.6.

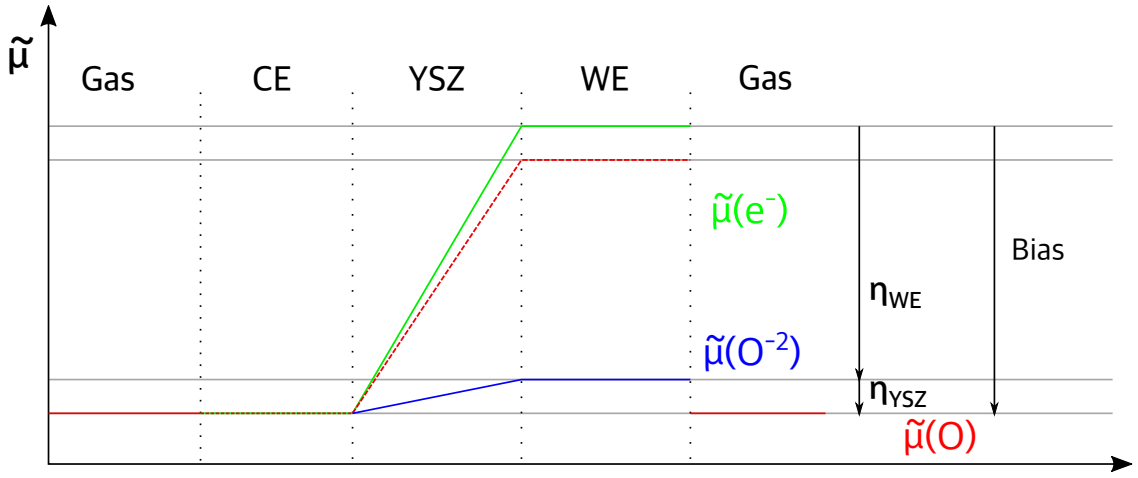

Figure 2.6: The electrochemical potentials of oxygen (red), oxygen ions (blue) and electrons (green) in an idealized electrochemical cell, using a porous counter electrode and a schematic image of overpotential η_{WE} and its relation to η_{YSZ} and the applied bias.

In Fig. 2.7 a sketch of a voltage-current characteristic (I-V curve) for an ideal system is shown where the I-V curve is visualised in blue and the part of the curve that is measured during AC measurement is marked in red. The current can be assigned to the net reaction of the described system.

In this thesis the current density is plotted versus the overpotential of the corresponding working electrode to create an area independency and thus give the opportunity to compare samples with different areas. Considering the relation be-

tween net reaction rate and measured current density and proportionality of η_{WE} and ΔG the slope of the resulting U-I curve equals a measure for the reaction rate, which is triggered by the applied bias.

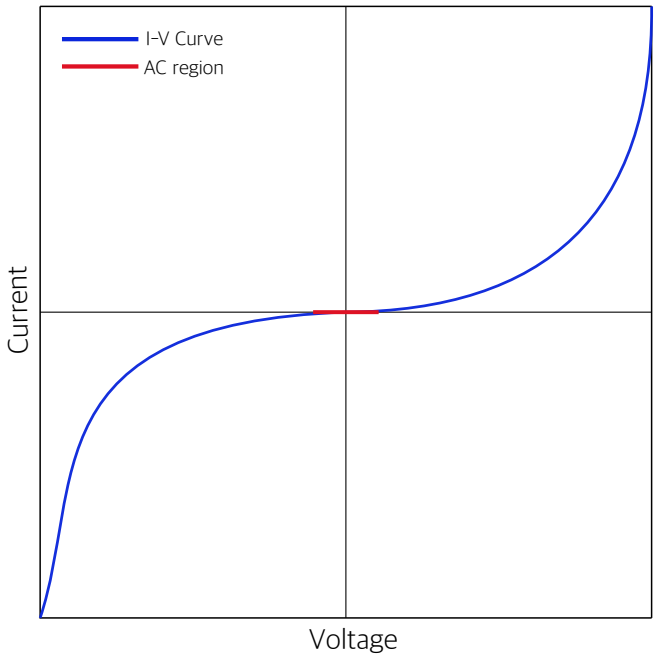

Figure 2.7: The voltage current characteristic curve of a electrochemical reaction in blue and in red the region for AC measurements

Moreover, there is also a relation between oxygen partial pressure and overpotential via the Nernst's equation, see Eq. (2.38). Due to the DC bias, the oxygen chemical potential in the electrode is not in equilibrium with the oxygen partial pressure of the gas phase see also Fig. 2.7. Considering Eq. (2.38) the overpotential can be transformed to a pressure ratio $(\frac{p1}{p2})$, where R denotes the ideal gas constant,

z the charge (for O_2), F the Faraday constant and p_1 and p_2 a partial pressure.

$$\eta = \frac{RT}{zF} * ln(\frac{p_1}{p_2}) \tag{2.38}$$

As a result an equivalent oxygen partial pressure can be defined, as shown in Eq. (2.39). This oxygen partial pressure equals to reducing or oxidizing conditions by applying a certain bias, which leads to an overpotential.

$$p_{eqv.} = p_{gas} * e^{\frac{\eta zF}{RT}} \tag{2.39}$$

3 Experimental

3.1 Target Preparation

Throughout this thesis, model electrodes with precise stoichiometry were required to determine each perovskite's exsolution behaviour. The model electrodes consist of a thin film working electrode (WE) prepared by pulsed laser deposition (PLD), a single crystalline YSZ electrolyte, and a brushed multilayer counter electrode (CE). Tab. 3.1 shows the stoichiometry and abbreviation of each perovskite target used for PLD deposition.

Table 3.1: Names and stoichiometry of the synthesised targets

Abbreviation	Stoichiometric Composition	Source	Synthesised by
LSF	$La_{0.6}Sr_{0.4}FeO_3$	synthesised in-house	Alexander Schmid
NCF	$Nd_{0.6}Ca_{0.4}FeO_3$	synthesised in-house	Melanie Maurer
NCFCo	$Nd_{0.6}Ca_{0.4}Fe_{0.9}Co_{0.1}O_3$	synthesised in-house	Harald Summerer
NCFCu	$Nd_{0.6}Ca_{0.4}Fe_{0.9}Cu_{0.1}O_3$	synthesised in-house	Melanie Maurer
NCFNi	$Nd_{0.6}Ca_{0.4}Fe_{0.9}Ni_{0.1}O_3$	synthesised in-house	Melanie Maurer

The powders for the targets were synthesised via the Pechini method [48]. The amount , purity and supplier of the chosen precursors are listed in Tab. 3.2.

Table 3.2: Weighted starting materials, their supplier, and purity used in the Pechini method

	NCF (g)	NCFCu (g)	NCFNi (g)	Supplier	Purity
Nd_2O_3	7.335	7.410	7.361	Alfa Aesar	99.997 %
CaO	2.900	2.939	2.921	Sigma Aldrich	99.995 %
Fe	4.058	3.690	3.667	Sigma Aldrich	99.98 %
$Cu(NO_3)_2$	0	1.707	0	Sigma Aldrich	99.99 %
$NiNO_3$	0	0	2.121	Sigma Aldrich	99.99 %

At first, for the respective materials all components were weighted and separately dissolved in diluted HNO_3 (65 % Merck.). In the next step, the solutions were mixed together in a quartz beaker and after addition of citric acid in a ratio of 1:1.1 (i.e. 10 % excess with respect to the cations) a complex was formed. Then, upon heating H_2O was evaporated until the mixture turned into a gel and after further heating self-ignition took place. The resulting black powders were calcined for 3 h at 800 °C and grounded afterwards. The powders were uniaxially pressed (4 kbar) and sintered at 1250 °C for 12 h. The targets were ground in one side by hand with SiC paper and an X-ray diffraction analysis (XRD) was performed on each target to confirm phase purity.

3.2 Sample Preparation

3.2.1 Counter Electrodes

The work flow of counter electrode preparation is shown in Fig. 3.1.

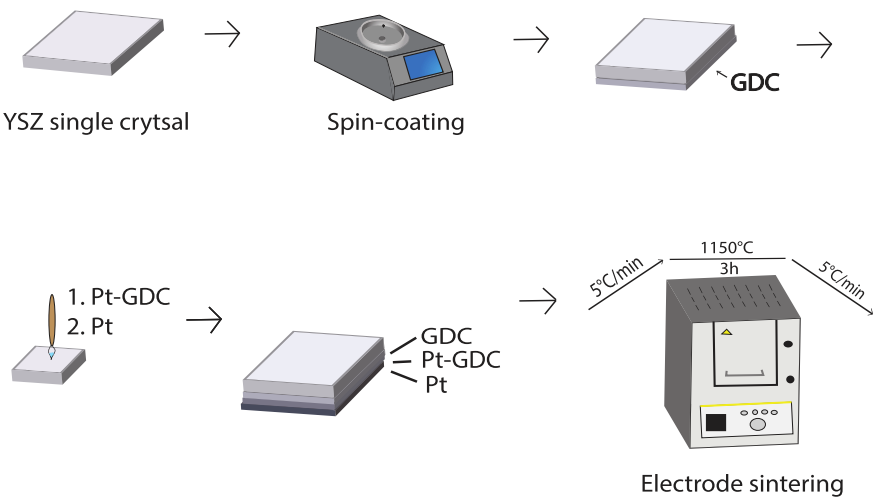

Figure 3.1: Illustration of the steps required to prepare the counter electrodes of the used samples on the yttria stabilized zirconia (YSZ, 100) single crystal (10 mm x 10 mm x 0.5 mm) as an electrolyte: spin-coating gadolinid-doped ceria (GDC), brushing the Pt/GDC and Pt layers and sintering the electrodes

In the first step, the counter electrode was brushed on a single side polished yttria stabilized zirconia (YSZ, 100) single crystal (10 mm x 10 mm x 0.5 mm), obtained from Crystec (Germany). The first applied layer was gadolinia-doped ceria (GDC), which was applied via spin coating on the non-polished side of the substrate. The GDC layer was dried for 10 - 15 min at 120 °C. A paste containing a mixture of Pt

and GDC was brushed on top of the GDC layer. Lastly, a layer of diluted Pt paste was applied and dried. Afterwards the multilayer electrode were sintered at 1150 °C for 3 h in air (heating and cooling ramps 5 °C/min) .

3.2.2 Working Electrodes

An illustration of the entire workflow required to prepare the working electrode is shown in Fig. 3.2.

To provide sufficient electronic current collection, a buried thin film grid was prepared via sputter deposition (MED 020 Coating System machine BAL-TEC Germany) of Ti/Pt. The Ti layer was applied first to provide a better adhesion of the layer on the polished side of the YSZ single crystal. The deposition parameters and resulting thickness of each layer are listed in Tab. 3.3.

Table 3.3: Deposition parameters for the sputter process of Ti and Pt

	Parameters:	**Sputtering**
Target	Titanium	Platinum
Target distance (cm)	6	6
Sputter current (mA)	100	100
Argon pressure (mbar)	7.3 *10^{-3}	2 *10^{-2}
Sputter time (s)	55	160
Layer (nm)	5	100

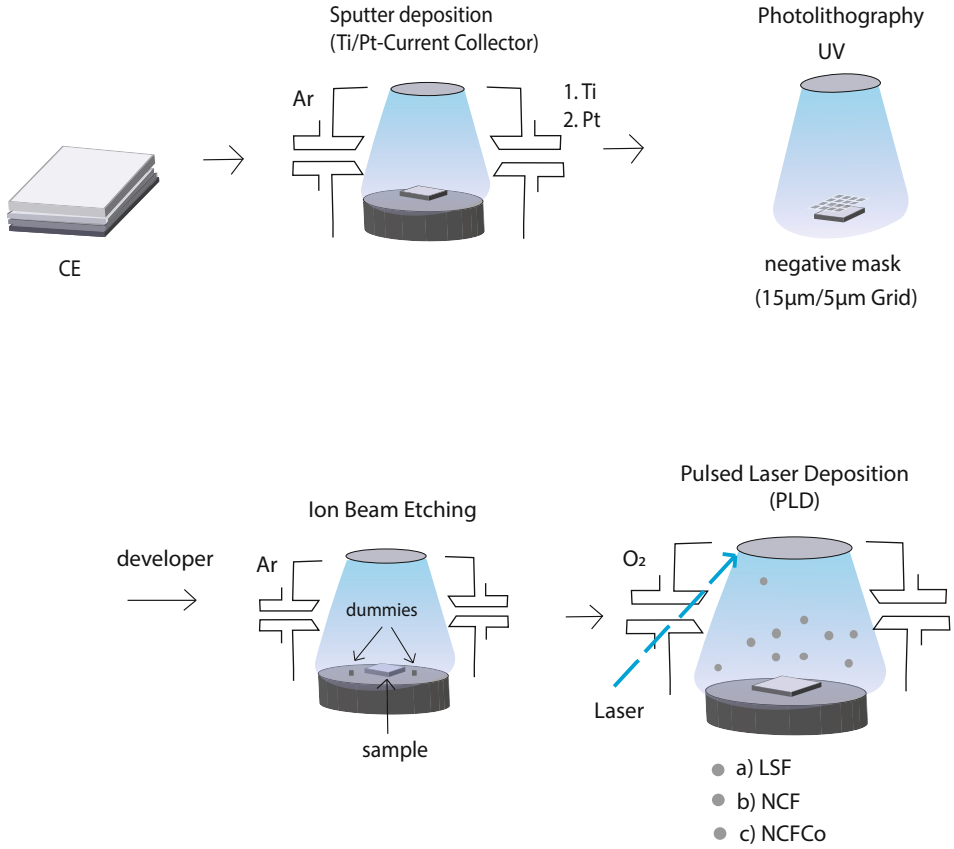

Figure 3.2: The preparation steps of the working electrodes: Ti/Pt sputter deposition, photolithography, IBE and pulsed laser deposition of the respective target (LSF, NCF, NCFCo)

From the Ti/Pt thin film a grid (5 µm strips, 15 µm spacing) was created via photolithography followed by ion beam etching (IBE). In the first step, a photoresist (N-1430 MicroResist Technology, Germany) was applied via spin-coating (SCC-200 KLM, Germany) onto the sputtered Ti/Pt layer. After about 4 min of prebaking (100 °C), a mask for the desired grid was applied. The resist was polymerised by ex-

posure to UV light for 1 min (350 W,USHIO 350DP, Hg, Ushio, Japan). To remove the uncured photoresist, the sample was put into a developer solution (MircoResist Technology, Germany). The parameters of all steps are shown in Tab. 3.4.

Table 3.4: Set parameters during the photolithography

Parameters:	**Photolithography**
Photoresist volume (µl)	100
Spincoater (speed/duration)	160 rps/120 s
Developing time (s)	37 - 40

In the next step, the samples were etched using Ar plasma. The parameters of this procedure are shown in Tab. 3.5. After IBE, the samples were rinsed with ethanol in order to remove residual photoresist. In Fig. 3.4 a magnified sample after ion beam etching (IBE) is shown. In the past, the grid was created via lift-off photolithography. However, this technique brings specific problems with it. The Pt-grid can, because of its structure, not be fully covered by the working electrode in the following step. Therefore, part of it penetrates the subsequently deposited perovskite film, hence providing free Pt on the surface. This masks the catalytic activity of the actual catalytic species, which should be observed in the measurements (see Fig. 3.3). Due to this problem, the sample preparation was done by to photolithography in combination with IBE.

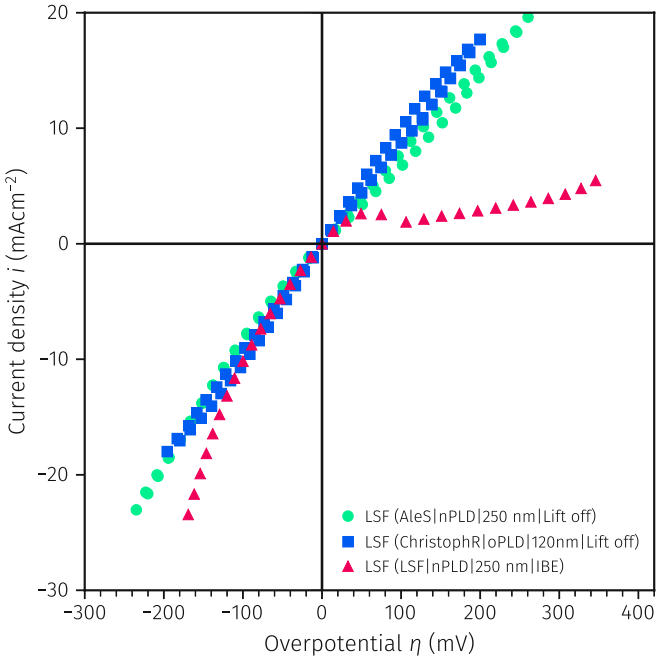

Figure 3.3: I-V curve of three samples, two were prepared with the lift-of technique (shown in green and blue) and on sample with photolithography in combination with IBE (shown in red)

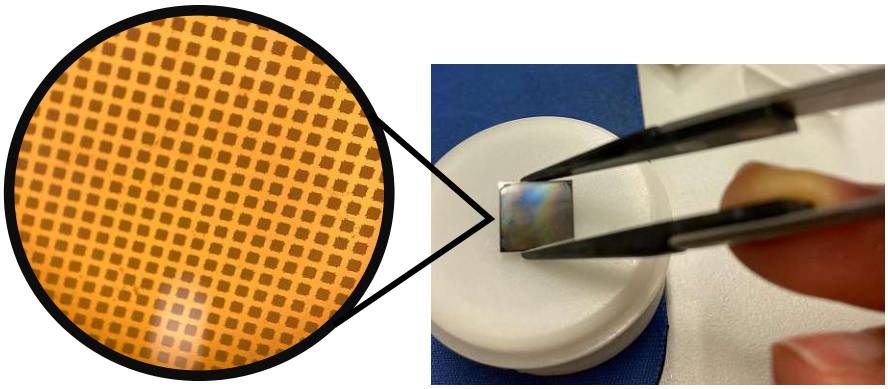

Figure 3.4: Sample after IBE and a magnification with a light microscope of the created Pt grid (5 µm strips, 15 µm spacing)

Table 3.5: Set parameters during ion beam etching

Parameters:	Ion Beam Etching
Magnetron current (mA)	150
Beam voltage (V)	400
Ar pressure (mbar)	$9*10^{-4}$
Plasma current (mA)	15
Etching time (min)	10

To ensure that the IBE process was completed, three dummy samples were placed next to the actual samples. These dummies were YSZ single crystals (5 mm x 5 mm x 0.5 mm) coated in the same sputtering process as the samples. Owing to the occurrence of the characteristic fluorescence when the Ar beam hits YSZ, these dummies are used to identify, when the YSZ subtract of the actual sample is exposed by comparing the fluorescence colour.

In the final step, the desired working electrodes were deposited by PLD. The PLD parameters can be found in Tab. 3.6. A Kr/F excimer laser (COMPex Pro 201F) was used to ablate the respective targets. A diamond scriber was used to create predetermined breaking points to break the sample into four roughly evenly sized pieces.

In Fig. 3.5 a sketch of a completed sample, containing CE, YSZ and WE is shown.

Table 3.6: Set parameters during PLD deposition

Parameters:	**Pulsed Laser Deposition**
Laser wavelength (nm)	248
Laser energy (mJ)	380 - 400
Pulse frequency (Hz)	10
Deposition time (min)	30
Deposition temperature (℃)	600
O_2 partial pressure (mbar)	0.04
Substrate to target distance (cm)	6

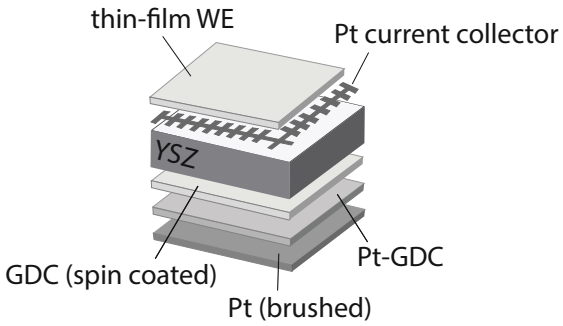

Figure 3.5: Sketch of the resulting samples

3.3 Measurement Setup

For all electrochemical experiments the same setup, shown in Fig. 3.6 and Fig. 3.7, was used. It consisted of a tube made out of quartz glass and a tube furnace (Gero, SR 40-200/12), which was required to achieve a constant temperature of 600 °C. The contacting apparatus consist of a hollow rod of fused silica, covering the sample holder. The samples were clamped between Pt-foil and meshes, which functioned as current collectors, wrapped around quartzglass spacers. In addition, a stamp with a spring mechanism was used to press both current collectors together, between which the sample was clamped. A two-wire measurement setup was used to contact the sample, each lead to one electrode of the sample. The Pt-foil and meshes were connected via Pt-wires to BNC connectors. The temperature was measured with a Type-S thermocouple which was placed near the sample. The entire system was mounted on a steel flange, that included the in- and outlets for feed gas. The final measurement setup is shown in Fig. 3.6. The sample holder, displaying the Pt-foil and meshes, and the stamp is shown in Fig. 3.7. In order to heat the setup, the tube was placed inside a tube furnace. Before heating the sample, the desired atmosphere was established and flushed for a few minutes. The set up could be connected to either a phase sensitive multimeter (PSM1735, by Newtons4th Ltd) with a Femto impedance converter or to a SourceMeter (SMU2611A, by Keithley) in order to enable the use of the same measurement setup in AC and DC measurements.

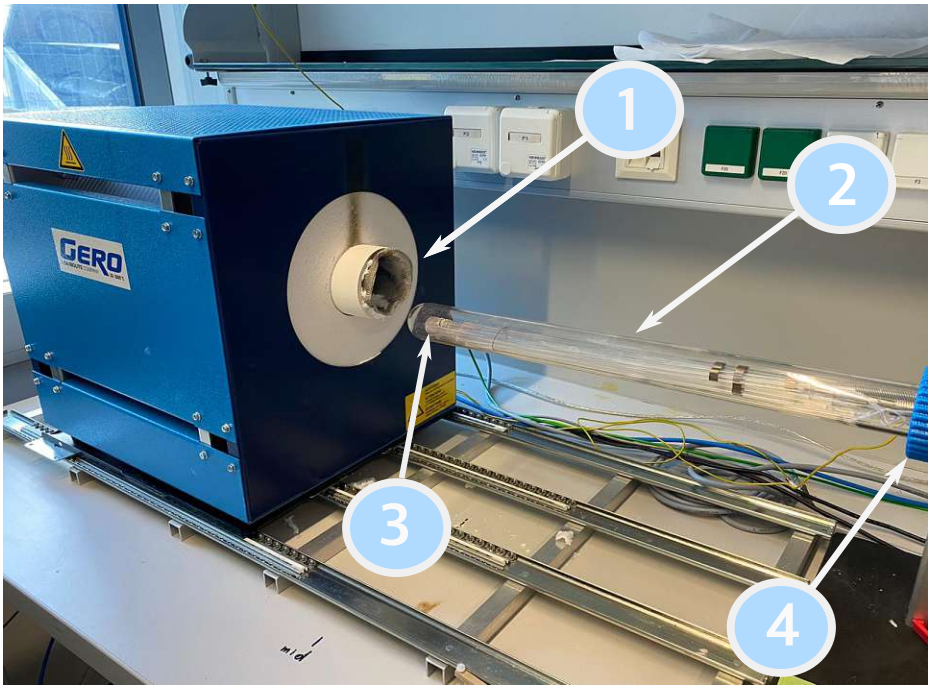

Figure 3.6: Image of the used tubular measurement setup. (1) tube furance (Gero, SR 40-200/12) (2) tube made of quartz glass (3) sample holder (4) 3D printed thread

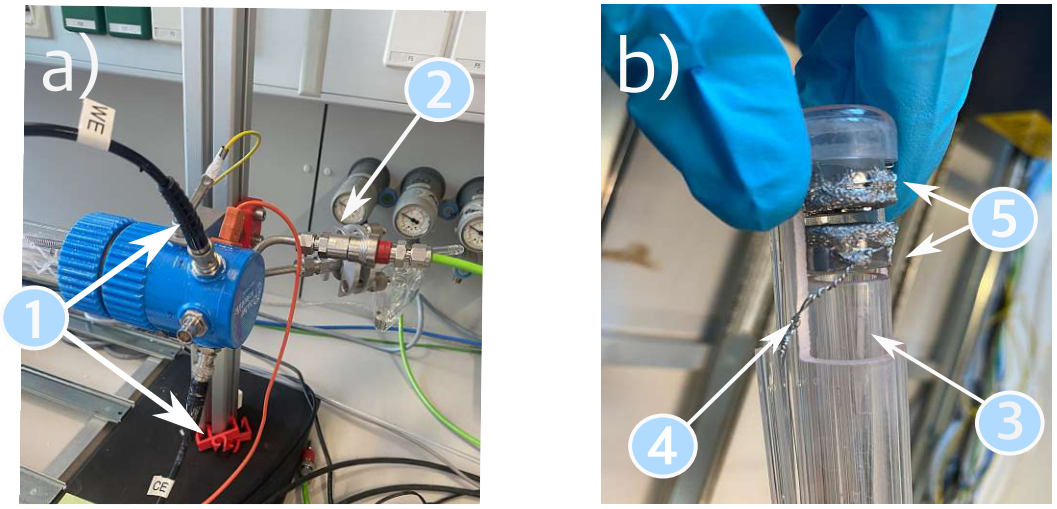

Figure 3.7: a) Electrical feedthroughs for the electrodes (1) and in- and outlets for gas (2). b)Image of the sample holder consisting of (3) the stamp (4) Pt-wires and (5) Pt-foil + mesh

Moreover, the opportunity to vary the atmosphere in the measurement setup was given. For this purpose the composition of the feed gas consisting of H_2 / Ar (2 % H_2, 98 % Ar) and Ar could be adjusted via a mass flow control system, the flow chart of this system is shown in Fig. 3.8. To enrich the Ar gas with H_2O it was lead through a humidifier filled with double distilled water. At standard condition (20 °C, 1 bar) a saturation is reached at partial pressure of ca. 25 mbar H_2O. Throughout this thesis is was necessary to conduct measurements in strongly reducing and oxidising environments (p (O_2) = 10^{-28} - 10×10^{-19} bar), and also measurement series at changing atmosphere were performed in the same apparatus.

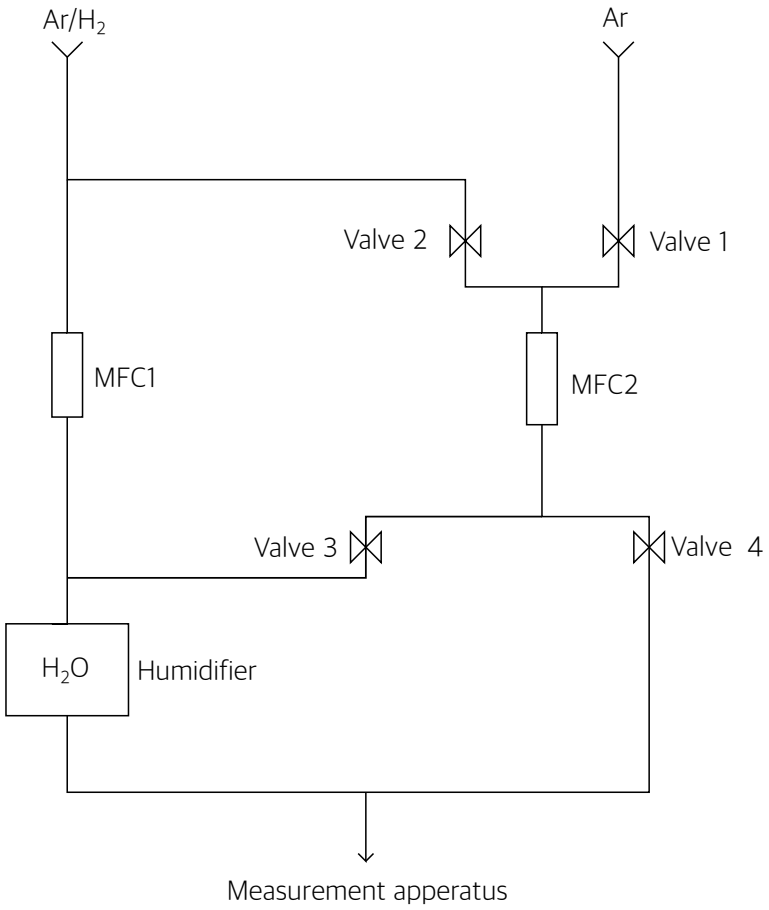

Figure 3.8: Flow chart of the used mass flow system: two gases can be introduced (Ar, Ar/H_2) and were regulated via 2 mass flow controller (MFC). With the help of four valves the way of the gases can be defined to make use of the different ranges of the two MFCs, humidifier is used to moisten the Ar gas

.

3.4 EIS Measurements

For each electrochemical experiment the sample was placed in the described measurement setup and heated up to 600 °C in the desired atmosphere. All EIS measurements were performed with a frequency ranging from 0.1 Hz to 10×10^6 Hz, with 10 points per decade resolution and an AC voltage of 10 mV toot mean square. The EIS measurements were performed before and after every DC measurement series in the same atmosphere as the first DC measurement of the corresponding series. For the conducted experiments a phase sensitive multimeter (PSM1735, by Newtons4th Ltd) with a Femto impedance converter was used.

3.5 DC Measurements

The measurement setup was the same as in the EIS measurements but it was connected to a SourceMeter (SMU2611A, by Keithley). During this thesis, two different kinds of DC measurement series were performed :

- Exsolution onset measurements
- $p(O_2)$ depending electrochemical switching

3.5.1 Determination of the Exsolution Onset

Due to a rapid change in the slope of the curve the change from catalytically active material to an inactive oxide can be determined. The goal was to evaluate the necessary cathodic bias when exsolutions first take place. Moreover, the onset potential was determined under varying measurement conditions and a further question was at which overpotential the electrochemical switching point can be observed for different onset conditions . This cathodic bias is referred to an onset potential.

Therefore, a method was created where the cathodic bias was gradually increased alternate with a measurement of the anodic branch of the I-V curve do detect the formation of exsolved metallic particles (see Fig. 3.9). The first measurement of the series was an I-V curve consisting of the anodic part, ranging from 0 mV to 400 mV. Then another I-V curve was measured starting with a cathodic bias of −25 mV and going up to anodic voltage of 400 mV. For the following measurements the maximal cathodic bias increased in −25 mV steps till −700 mV were reached. After each step, an I-V curve starting with the new maximal cathodic bias was recorded. An example of a resulting I-V curve is shown in Fig. 3.10. The region of interest, i.e. the part of the I-V curve where the electrochemical switching point was expected, was recorded in higher resolution (5 mV steps) as opposed to the standard 25 mV for the rest of the curve. The acquisition time of the applied anodic bias was 30 s and acquisition times of the applied cathodic bias was varied between 1 min and 60 min for different measurement series, to determine the influence of the holding time on the electrochemical switching point.

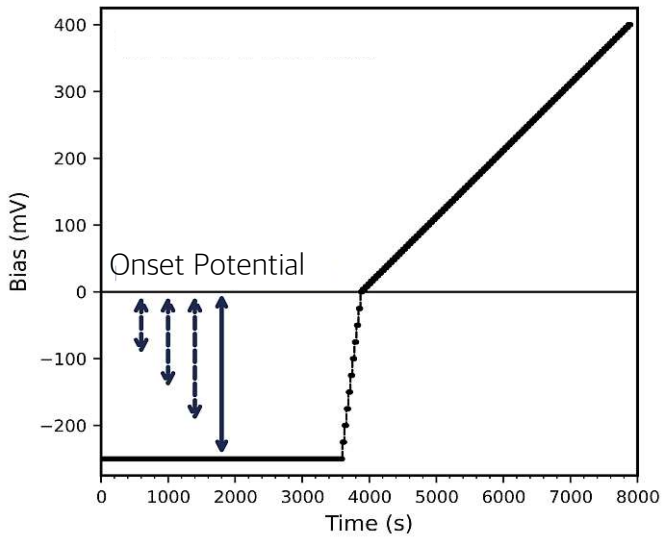

Figure 3.9: A function of the applied bias in mV over time in s and the onset potential

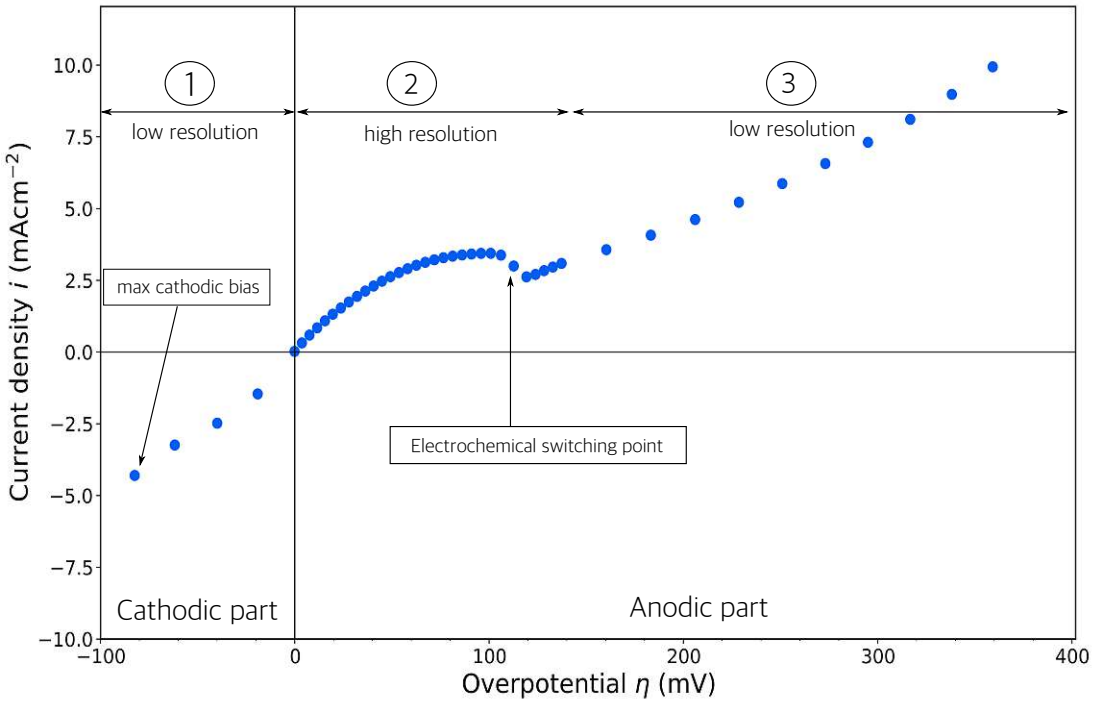

Figure 3.10: I-V curve of a sample, (1) presents the low resolution cathodic curve (step width 25 mV), (2) presents the high revolution part of the anodic curve (step width 5 mV) and (3) the low resolution 25 mV of the anodic curve

3.5.2 Oxygen Partial Pressure Dependence of the Electrochemical Switching Point

The purpose of the second measurement series was to analyse the electrochemical switching behaviour under different conditions. The electrochemical switching behaviour was investigated by recording I-V characteristic curves. The oxygen partial pressure dependence of the electrochemical switching point was investigated. For these measurements samples were used, which already carry exsolved particles on their surface. I-V curves were recorded in different atmospheres with an applied voltage ranging from −400 mV to 400 mV with an acquisition time of 30 s. The part of the I-V curve where the electrochemical switching point was expected due to thermodynamic data[1] (see Tab. 3.7), was recorded with a higher resolution, i.e. in 5 mV steps. This region of interest starts with the thermodynamic switching point and ends after additional 150 mV. The remaining part of the curve was measured with 20 mV voltage steps. The hydrogen content was stepwise changed from 1:1 (H_2:H_2O) (more oxidising) to 100:1 (H_2:H_2O) (more reducing) and then decreased to 1:1 (H_2:H_2O) again. In addition, measurement series in more oxidising conditions ranging from 1:1 (H_2:H_2O) to 1:100 (H_2:H_2O) were conducted in the same way as described above. To ensure a compllete gas exchange in the electrochemical setup flushing with the respective gas composition was carried out for 20 min before a measurement was stated in a ne atmosphere. The overall oxygen partial pressure range for both measurement series was 10^{-28} - 10×10^{-19} bar).

[1] provided by Ass.Prof. Dr. Raquel de Oro Calderon

Table 3.7: Thermodynamic switching points of Fe at 600 °C

Atmosphere (H_2:H_2O)	Thermodynamic switching point (mV)
1:1	-19
10:1	67
20:1	93
40:1	119
60:1	134
80:1	145
100:1	154

4 Results and Discussion

4.1 Target Characterisation via X-ray Diffraction

In order to ensure phase purity of the targets, X-ray diffraction measurements were performed. The targets were measured for 60 min in Bregg-Brentam geometry. The obtained diffractometer pattern of the NCF ($Nd_{0.6}Ca_{0.4}FeO_{3-\delta}$) target is shown in Fig. 4.1. As no matchable literature data was available, a comparison with an existing target prepared by Harald Summer was made and showed a good agreement.

In addition, a comparison with the ICSD database was made with a database between NCF and calcium iron neodymium oxide ($Ca_2Nd_2Fe_4O_{11}$), which is not equal to $Nd_{0.6}Ca_{0.4}FeO_{3-\delta}$ but very similar. The matching reflections are marked in Fig. 4.1. The refections, which could not be assigned to the data bank were also found in the reference of Harald Summerer. Moreover, no evidence of any other oxides like Fe-oxides or Nd-oxides could be found.

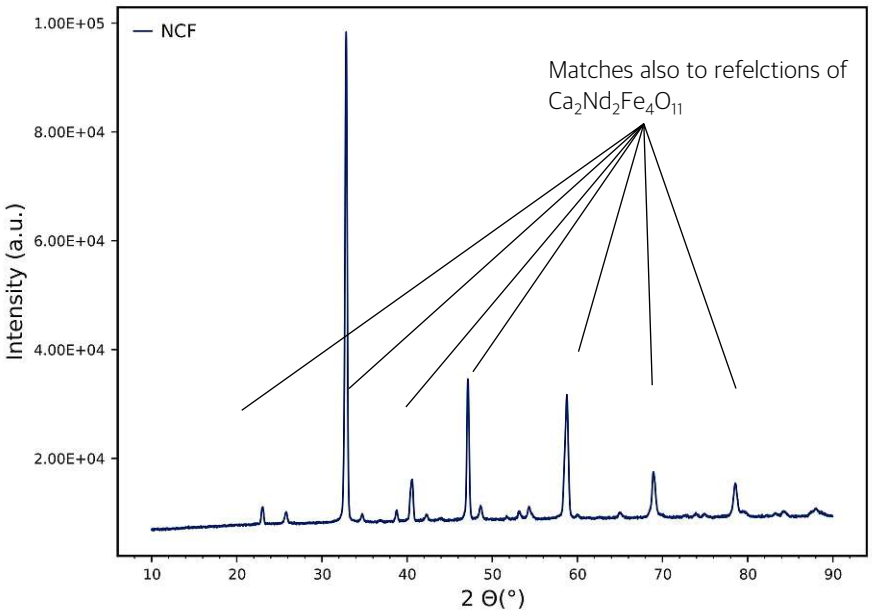

Figure 4.1: Diffraction diagram of NCF

4.2 Electrochemical Switching Behaviour

During all electrochemical experiments the model reaction of water splitting was used to analyse the behaviour of the thin film perovskite electrodes, shown in Eq. (4.1). For EIS measurements as already mention in Subsec. 2.5.1 the equilibrium of the respective reaction remains, thus $r_1 = r_2$.

$$H_2O + V_O^{\bullet\bullet} + 2e' \underset{r_1}{\overset{r_2}{\rightleftharpoons}} H_2 + O_O^{\times} \tag{4.1}$$

4.2.1 Determination of the YSZ Resistance

The complex impedance of the sample was measured as a function of the frequency, and a Nyquist plot was created. Therefore, the imaginary part of the impedance was plotted versus the real part in the complex plane as a parametric function of the frequency. A resulting EIS spectra of a NCF thin-film electrode measured in an atmosphere of 30:1 H_2:H_2O is shown in Fig. 4.2. Throughout the thesis, R_{YSZ} was around 40-60 Ω, depending on the exact size of the fragment of the sample after breaking it into quarters [49].

To determine the overpotential of the working electrode, it is necessary to define the resistance of the eYSZ electrolyte. Therefore EIS measurements were performed before every DC measurement to evaluate the YSZ resistance (R_{YSZ}). Ohm's law can be applied, since the electrolyte resistance is a purely ionic resistance, and it is possible to determine it by means of EIS measurements. To evaluate the electrode resistance the spectra were parametrised with an equivalent circuit. A simple equivalent circuit, consisting of a resistor in series with two R||CPE elements was chosen, as shown in Fig. 4.3. The resistance of the working electrode (R_{WE}) of the low-frequency R||CPE element describes the oxygen incorporation into the electrode [50]. From earlier work it is known that R_{WE} the resistance of the electrode surface reaction [51]. The capacitance of the R||CPE element describes the chemical capacitance C_{Chem}, which could be be attributed to oxygen stoichiometry changes in the bulk of the electrode [52].

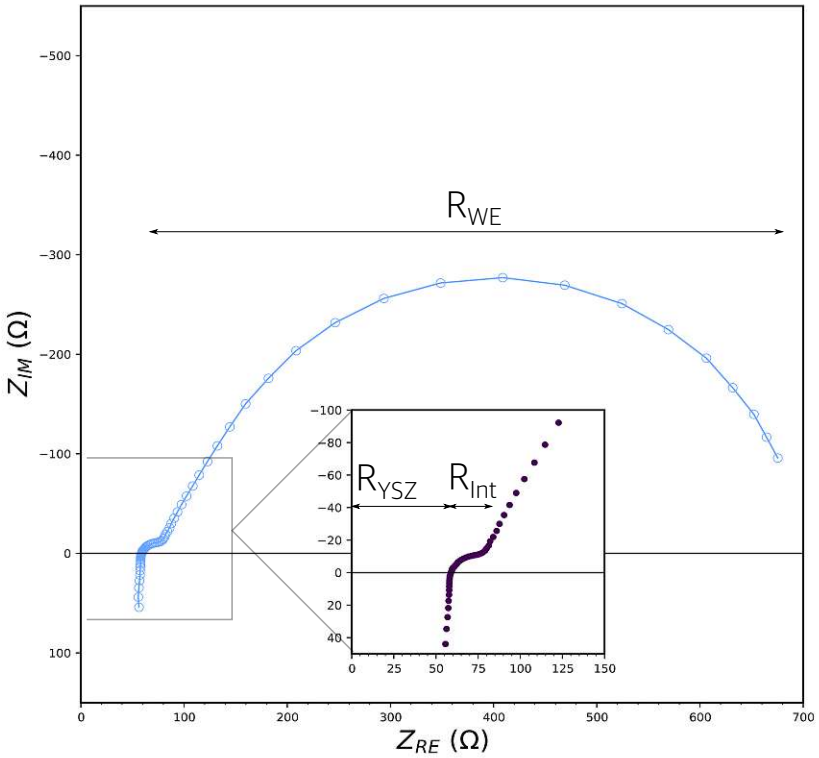

Figure 4.2: Nyquist plot of an typical EIS measurement: blue points show the impedance of an NCF sample measured in an atmosphere of 30:1 (H_2:H_2O), the purple points show only a small part of the identical spectra to visualize the offset resistance, and the interface. The lines are fits to the equivalent circuit describe in Fig. 4.3

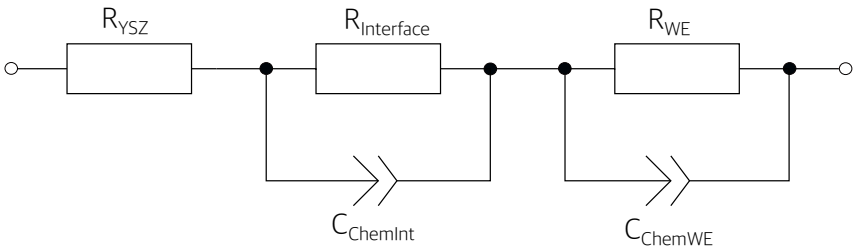

Figure 4.3: The used equivalent circuit used for determination of the electrochemical parameters of the samples

The resistance of the counter electrode is not visible in the spectra, because the used electrode is porous, i.e. the electrochemical active area is very large. Therefore the reaction on the counter electrode is very fast and does not cause a significant resistance. Thus, the determination of the resistance of the counter electrode was not necessary, which has already been analysed in a recent study [53]. In the medium frequency region a reactively small semicircle could be observed, which diameter equals the interface resistance (R_{Int}). Since this is very small, it was considered in the fit but not included in the determination of the resulting overpotential.

4.2.2 Results of the EIS Measurements

Before and after every DC measurement, 10 EIS spectra were measured without a bias voltage. For simplification, only the first, fifth and ninth spectrum was visualized in the further figures. In Fig. 4.4 these plots are shown for a LSF sample measured in atmospheres of 1:1 (H_2:H_2O) and 10:1 (H_2:H_2O).

Due to a smaller R_{WE} after the DC measurements formation of exsolved particles at the surface can be assumed. However, a change of the AC polarisation resistance alone was not seen as sufficient evidence for occurrence of exsolution. It was found that LSF does not show any exsolutions at an atmosphere of 1:1 (H_2:H_2O), as the reducing atmosphere alone do not yet provide sufficiently reducing conditions exsolutions. After DC measurements in an atmosphere of 10:1 (H_2:H_2O), exsolutions were indicated by AC measurement. Considering Fig. 4.4, it could be assumed that when no change of the surface activity has taken place and thus no exsolutions

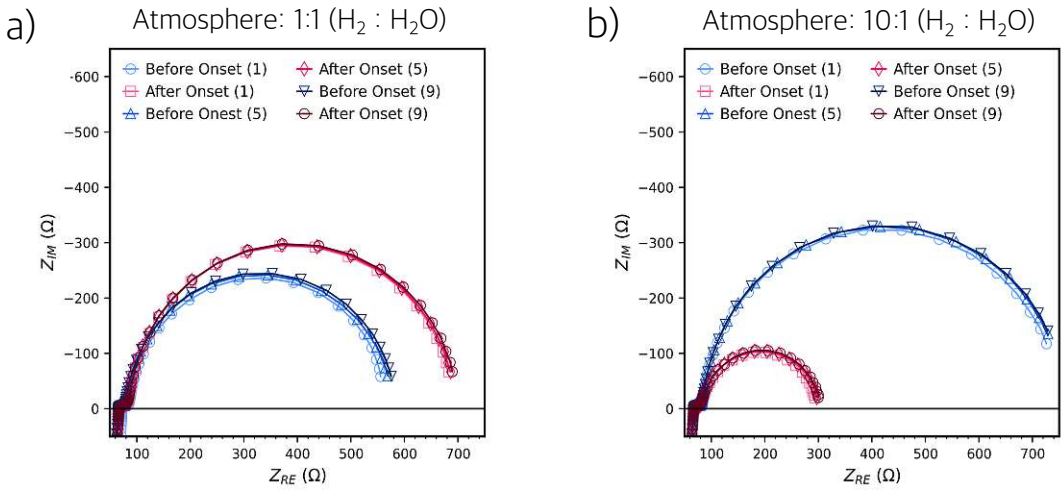

Figure 4.4: a) Nyquist plot of two EIS measurement series of a LSF electrode. The blue spectra were recorded before a DC measurement series was conducted (in a constant atmosphere 1:1 (H_2:H_2O). The red curve shows the AC measurements after the DC measurements were performed in the same atmosphere b) EIS measurement series before and after DC measurements were conducted in an atmosphere of 10:1 (H_2:H_2O)

were present the polarisation resistance of the working electrode (R_{WE}) remains in the same range before and after a DC measurement series was conducted, but when exsolution has been performed a significant decrease of R_{WE} was observed. It was noticeable that the R_{WE} value after showing exsolution always settled around 200-300 Ω. This behaviour can even be observed when the electrode resistance before the measurement is over 1000 Ω,i.e. for already degraded electrodes, see Fig. 4.5. This EIS measurement series was performed in an atmosphere of 30:1 H_2:H_2O.

In the last part of the experiments A- and B-site doped perovskites were analysed (NCFCo). Due to the easier reducibility of Co, in comparison to Fe, an atmosphere of 1:1 H_2:H_2O is already sufficiently reducing to cause exsolutions. Since, there

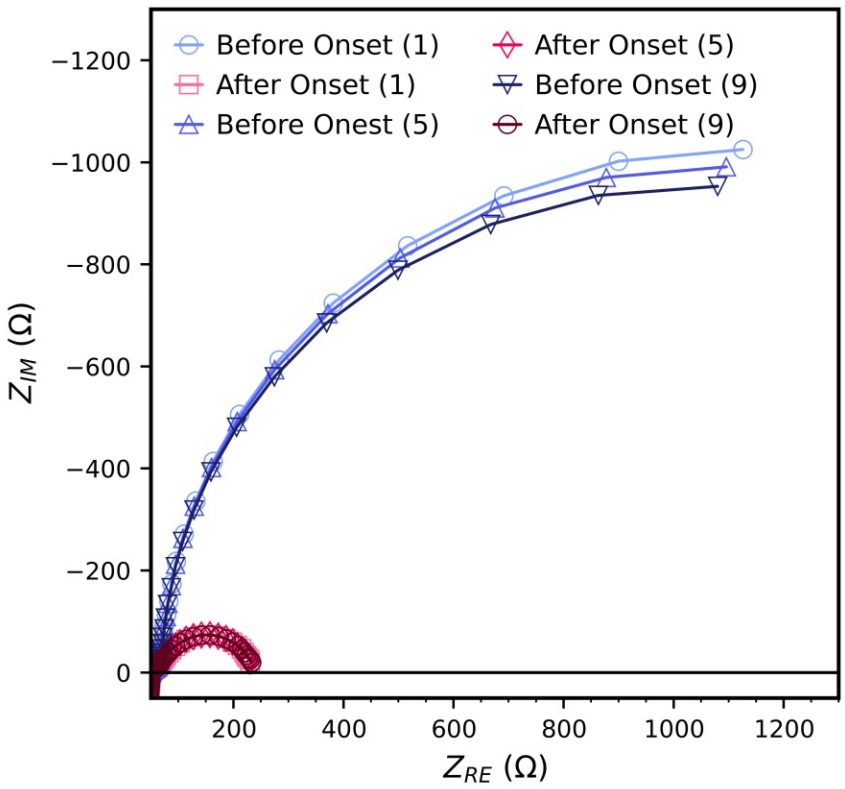

Figure 4.5: Nyquist plot of an LSF electrode, the blue points show the measured spectra before DC measurements were performed and the red points afterwards (atmosphere = 30:1 (H_2:H_2O)

was no significant change in R_{WE}, as shown in Fig. 4.6, i.e. it could be assumed that metallic Co particles were already present on the surface of the electrode from the start of the measurement due to of the surrounding atmosphere even without bias.

Further measurements of NCFCo were performed in an atmosphere of 10:1 H_2:H_2O, as shown in Fig. 4.7. In contrast to the previous measurements of LSF and NCF, a slightly higher surface resistance (R_{WE}) was found after DC measurements.

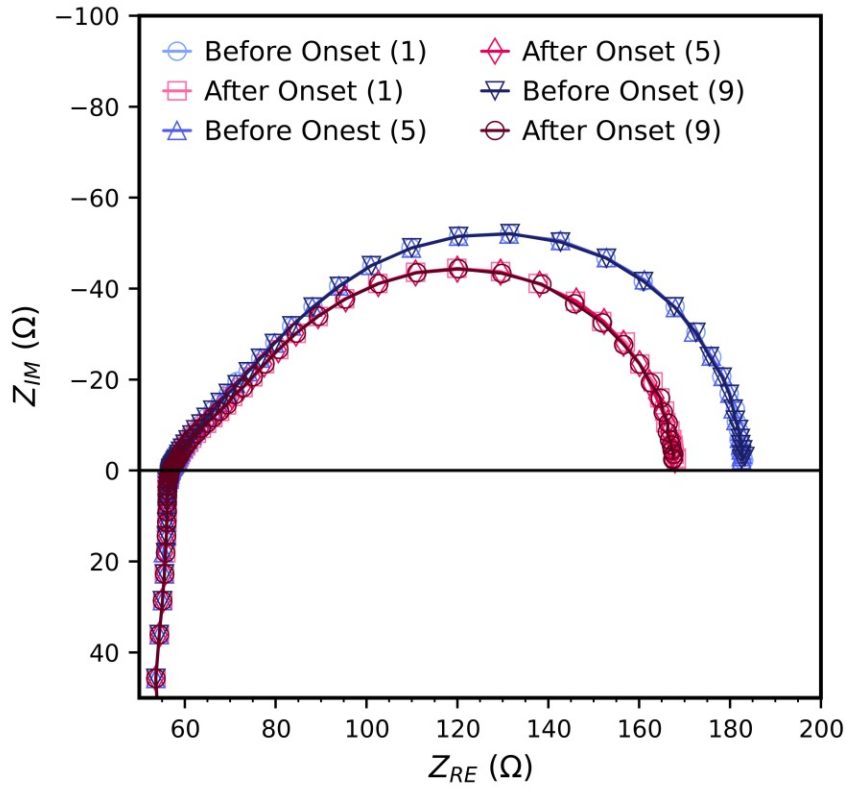

Figure 4.6: Nyquist plot of NCFCo; The blue curves show the spectra before a DC measurement was conducted and red curves afterwards (atmosphere = 1:1 (H_2:H_2O))

4.2.3 Analysis of the Exsolution Onset Potential

Determination of the Exsolution Onset

The aim of these experiments was to find the exsolution onset potential, i.e. the cathodic bias that under certain reaction condition is needed for the electrode to show exsolutions and to achieve a better understanding of the electrochemical switching behaviour of perovskite-type electrodes, which already posses exsolution on its surface. For DC measurements in general, the respective reaction remains no

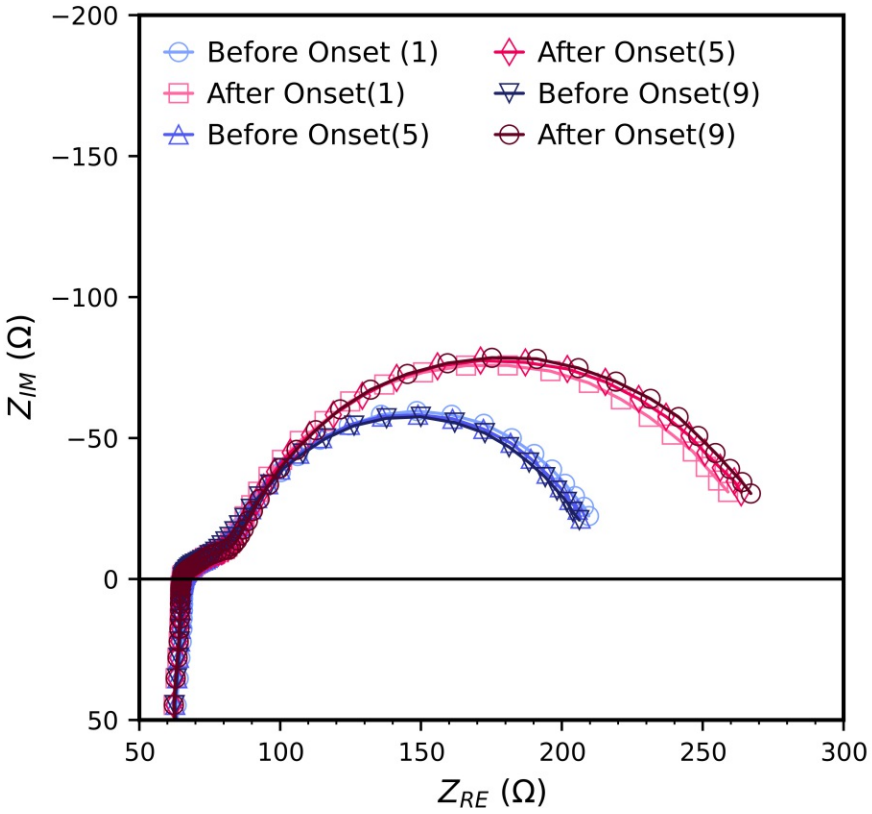

Figure 4.7: Nyquist plot of NCFCo the blue curves show spectra before DC measurements were conducted and the red curves after DC measurments were conducted(atmosphere = 10:1 (H_2:H_2O))

longer in its equilibrium, in this case the reaction described in Eq. (4.1) was used as an example and thus $r_1 \neq r_2$. The steady state of the reaction is controlled by the applied voltage. The reaction rate is given by the resulting current according to the Farday's law as explained in Subsec. 2.5.2.

Therefore, I-V curves can be used as an excellent indicator whether a reaction has a high or low net reaction rate and thus they allow to recognise changes in the reaction behaviour of a system, e.g. inactivation and activation of a catalytic species on the surface of a mixed conducting electrode. For this purpose, this behaviour is explained with exsolved Fe particles sitting on the surface of a LSF electrode as an

example. For a steeper slope in the I-V curve (= lower differential resistance) the presence of a catalytically active species such as Fe^0 can be assumed on the surface of the electrode. In contrast, a rather flat slope indicates the presence of Fe-oxide [34, 35]. Therefore, a rapid change in slope indicates a change from Fe^0 to Fe-oxide, as shown in Fig. 4.8 for a sample with a LSF working electrode. The anodic part of a I-V curves was used during this thesis as a tool to indicate whether exsolution has taken place. An abrupt change in the slope was defined as the electrochemical switching point. The applied cathodic bias, on the other hand, can trigger further exsolutions at sufficiently reducing conditions.

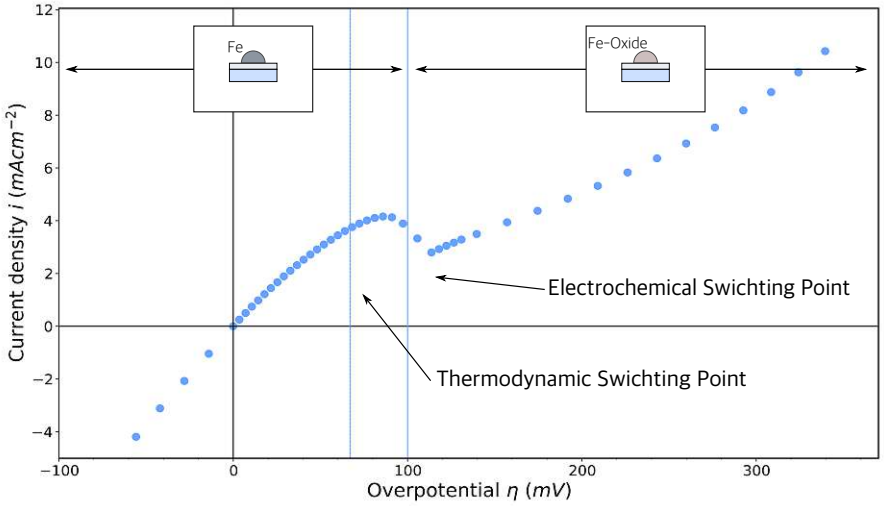

Figure 4.8: I-V curve for a sample with a LSF working electrode (atmosphere = 10:1 (H_2:H_2O)) showing electrochemical switching of Fe to Fe-oxide.

Results show that the electrochemical switching point was observed at a higher overpotential than a calculated thermodynamic switching point. In order to receive the thermodynamic switching point data from Ass.Prof Dr. Raquel de Oro Calderon

were used. Thus, a kinetic limitation of the electrochemical oxidation reaction can be assumed that causes a need of higher anodic overpotential to oxidise Fe^0 to Fe-oxide, also shown in Fig. 4.8.

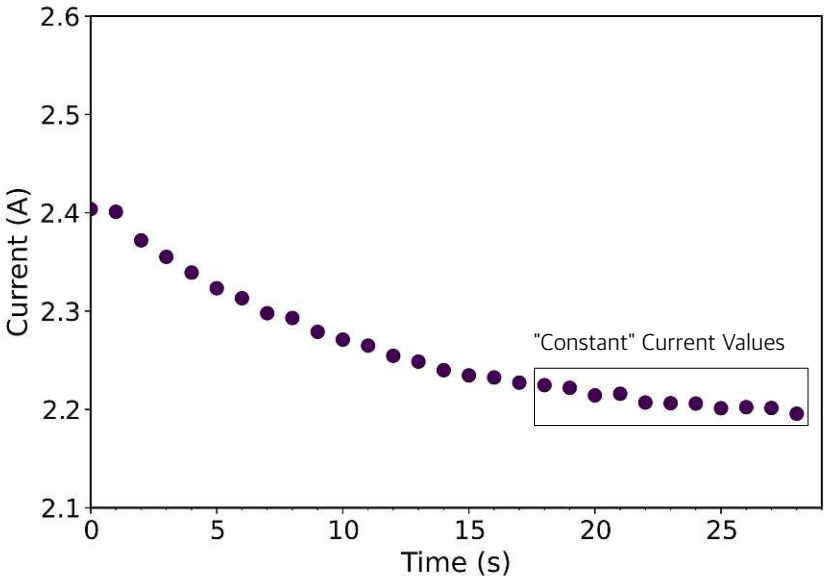

Figure 4.9: Current values over time at a constant voltage during a DC measurement; the used ”constant” current values for the further evaluation

To create the I-V curves correctly, the applied voltage needed to be converted to the overpotential (η_{WE}) as shown in Subsec. 2.5.2. The current (mA) was converted into a current density by dividing it by the active area (cm^2) of the measured sample to get area independent data so that samples with different areas could be compared. When voltage is applied, the resulting current initially decreases and then settles on a constant value after a few seconds, this behaviour is shown in Fig. 4.9. Therefore an average of the last ten current values was used in the further analysis.

In the following I-V curves, the maximum of the previously applied cathodic bias can be found in the upper left corner and only the subsequently measured anodic part of the I-V curve is visualized. An example of a DC measurement series is given in Fig. 4.10, showing six I-V curves of a sample with a LSF working electrode measured in an atmosphere of 30:1 H_2:H_2O. For one measurement series, 29 I-V curves were recorded, as described in Subsec. 3.5.1. In the following chapter, always only selected representative data are shown.

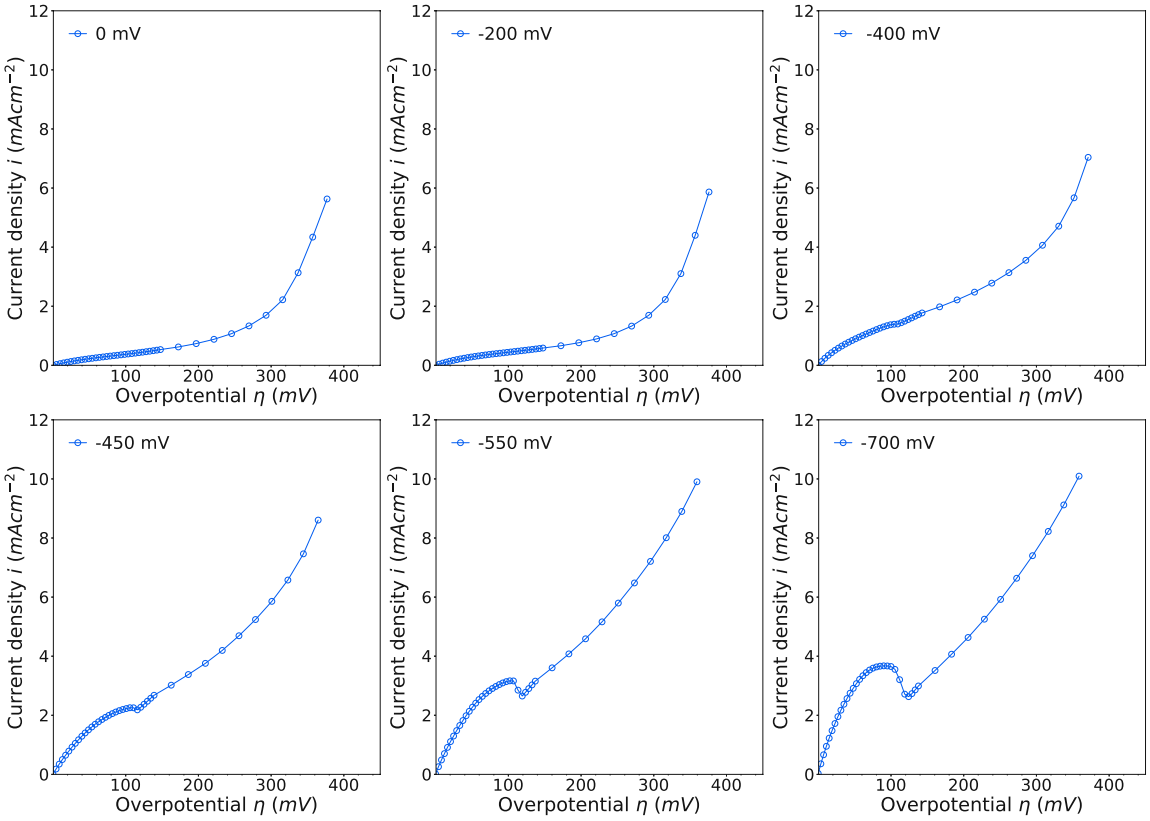

Figure 4.10: I-V curves of a sample with a LSF working electrode measured in an atmosphere of 30:1 H_2:H_2O. Cathodic bias values of 0, -200, -400, - 450, -550 and -700 mV were applied for 60 s before measuring the respective anodic part of the I-V curve.

The DC measurements were performed on samples with different thin film electrodes in various atmospheres, shown in Tab. 4.1.

Table 4.1: Parameters for the exsolution onset measurements

	LSF	NCF	NCFCo
H_2:H_2O	1:1	1:11	1:1
H_2:H_2O	10:1	10:1	10:1
H_2:H_2O	30:1	30:1	

Influence of Atmosphere and Time on the Exsolution Onset Behaviour

In order to get a further insight into the exsolution onset behaviour, the prepared samples were analysed in varying reaction condition. In Fig. 4.11 a comparison of two samples with a LSF thin film electrode in an atmosphere of 30:1 H_2:H_2O with an onset hold time of the cathodic bias of either 1 min (blue) or 60 min (red) are shown. As can be seen in Fig. 4.11 the electrochemical switching point appears already at −450 mV after long cathodic polarisation (60 min) and at −650 mV after short polarisation (1 min). A very similar behaviour, for the onset potential and the electrochemical switching point was found for samples with NCF thin film electrodes. Despite the very different onset behaviour, as soon as exsolutions were present, the electrochemical switching point appeared always at the same overpotential, irrespective of the sample pre-history. This means that the electrochemical switching point is independent of the duration of the applied cathodic bias. In Fig. 4.11 this

independence of the switching potential from the experimental pre-history is not only true for different exsolution condtiond, but especially for different states of degradation of the perovskite surface. The resulting different activities of the bare LSF electrodes became noticeable through the fact that the slopes of the I-V curves before exsolution differ strongly, which indicates very different reaction rate. This behaviour, however, did not impact the bias necessary to reach the electrochemical switching point. Taking this into consideration, the electrochemical switching point was not influenced by the surface activity (and thus by the surface condition of the bare LSF electrodes).

An example of a DC measurement series with LSF thin film electrodes in two different atmospheres but with the same acquisition time is shown in Fig. 4.12. A Comparison of the I-V curves measured in different atmospheres, showed that the electrochemical switching points appeared at different overpotentials and required different onset potentials. The electrochemical switching point of the I-V curve of the sample recorded in an atmosphere of 30:1 H_2:H_2O (blue) appeared after a polarisation of −450 mV at an overpotential of 110 mV. The electrochemical switching point of the I-V curve of the sample in an atmosphere of 10:1 H_2:H_2O (red) appeared after a polarisation of −650 mV and at an overpotential of 75 mV. This result shows that in more reducing atmospheres -as expected- less cathodic bias is requried to trigger exsolutions, i.e. had a lower onset potential. Moreover, a shift of the electrochemical switching point to more anodic values could be observed, which is also in accordance with the expectation that more electrochemical driving force is need to compensate for the more reducing atmosphere. The relationship between the

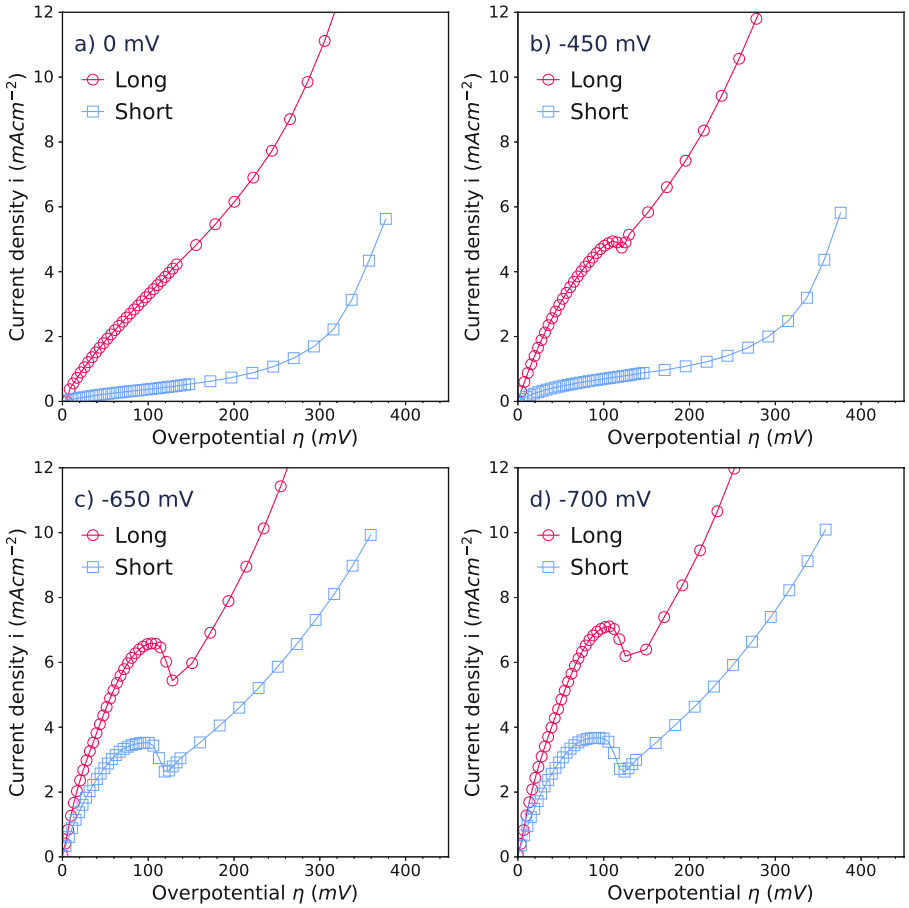

Figure 4.11: I-V curves of two samples with LSF thin film electrodes recorded with either 1 min (blue) or 60 min (red) onset hold time of the cathodic bias in an atmosphere of 30:1 H_2:H_2O In addition, the blue curve show a degraded LSF, while the red data were recorded on a more active one. Never the less the switching point is identical.

overpotential of the electrochemical switching point and the oxygen partial pressure is described in more detail in Subsec. 2.5.2. There, it is also shown that the shift can be described by the Nernst equation and the fact that an overpotential also shifts the oxygen chemical partial in the electrode. A very similar behaviour behaviour was observed for NCF thin-film electrodes, shown in Fig. 4.13.

In an atmosphere of 1:1 H_2:H_2O -i.e. under more oxidising conditions- both samples did not show any verifiable exsolution behaviour. At first sight this suggest that these reaction conditions were not able to reduce Fe-oxides to Fe^0 with −700 mV bias applied. However, thermodynamic calculation showed that the electrochemical switching point would not appear in anodic but in the cathodic part of the function, which means that the employed measurement mode could not identify the electrochemical switching point anyway. Hence, formation of exsolution could also not be excluded.

Influence of the Electrode Material of the Thin Film Electrode

Furthermore, a comparison of the exsolution behaviour of samples with NCF and LSF thin film electrodes was made. In Fig. 4.14 I-V curves of LSF (red) and NCF (blue) thin film electrodes in an atmosphere of 10:1 H_2:H_2O with onset hold time of the cathodic bias of 1 min are shown. NCF thin film electrodes showed an exsolution onset at lower cathodic polarization than samples with LSF thin film electrodes. However, when exsolution has been performed, the electrochemical switching point always appeared at the same overpotential. While the onset potential depends on the electrode material, the electrochemical switching point is independent of the electrode material. This behaviour indicates that for both materials the electrochemical switching point is caused by oxidation of Fe to Fe-oxide on the electrode surface, while the onset potential of the exsolution behaviour itself involves specific proprieties of the perovskit-type electrode material.

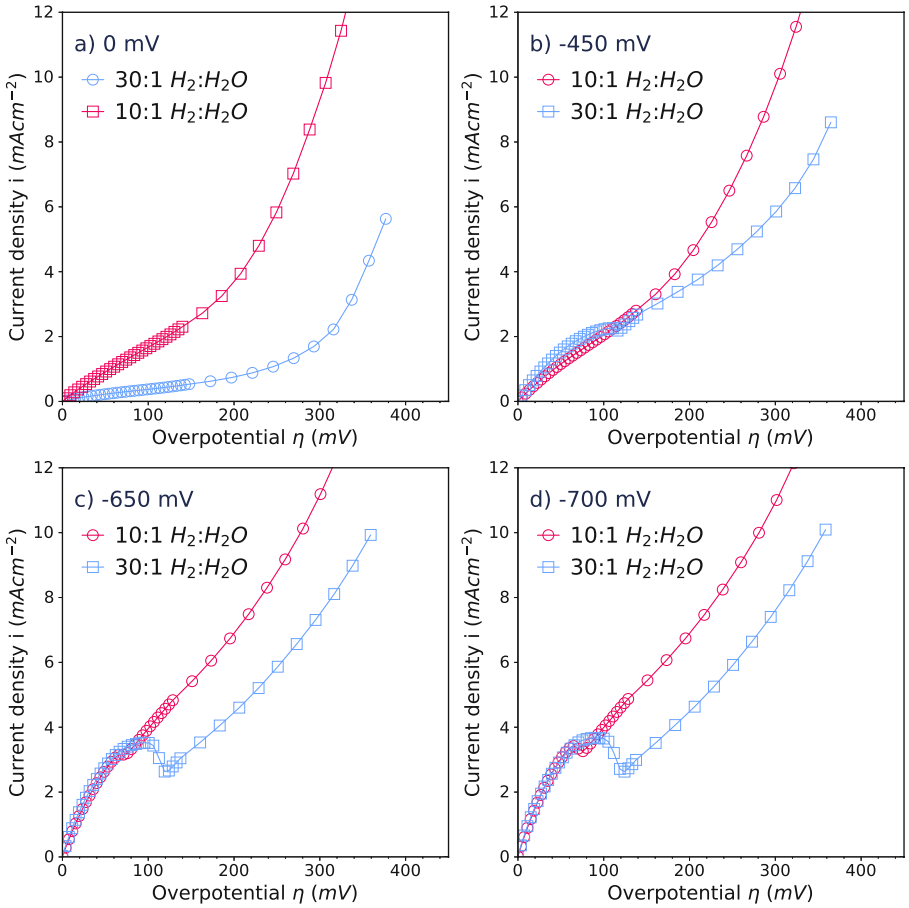

Figure 4.12: I-V curves of two different samples with LSF thin film electrodes measured with 1 min onset hold time of the cathodic bias in atmospheres of 10:1 (red) and 30:1 (blue) H_2:H_2O

As already mentioned, I-V curves of NCFCo were also measured, starting with an atmosphere of 1:1 H_2:H_2O and an onset hold time of 1 min. These conditions already led to exsolutions, without any applied cathodic bias as shown in Fig. 4.15. The electrochemical switching point hence already appeared in the very first I-V curve, where no cathodic bias was applied before. It can be assumed that Co^0 alone was exsolved due to the fact that in previous experiments with NCF Fe^0 was not formed in an atmosphere of 1:1 H_2:H_2O.

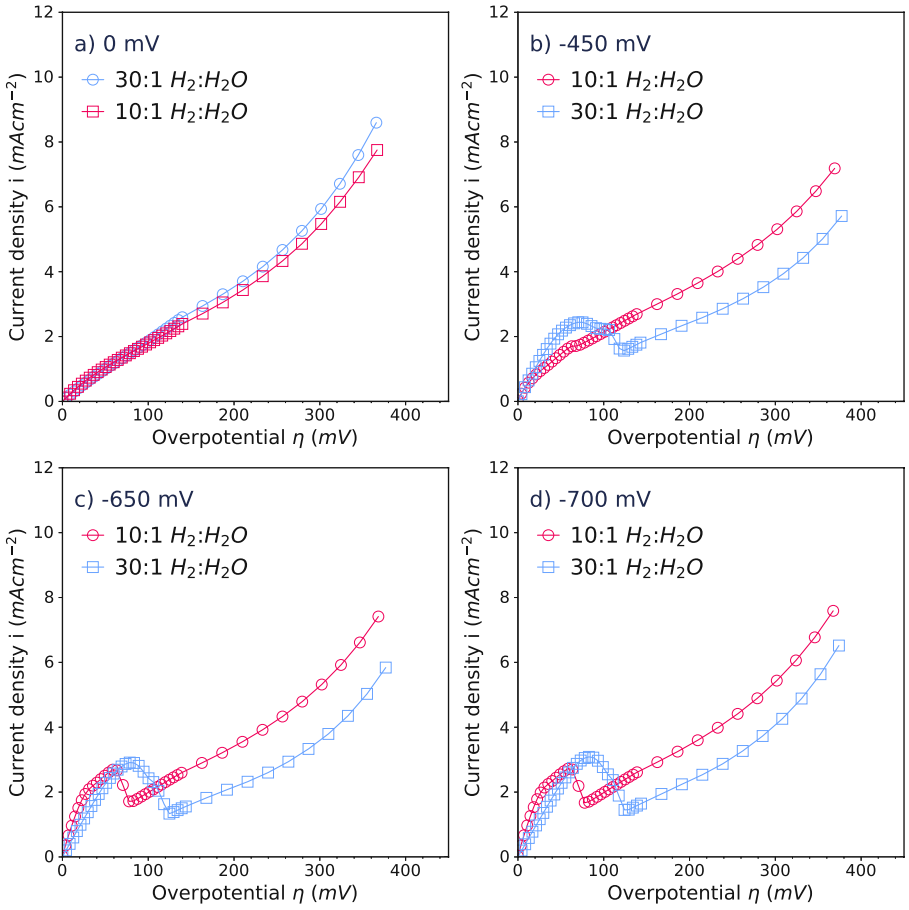

Figure 4.13: I-V curves of two different samples with LSF thin film electrodes measured with 1 min onset hold time of the cathodic bias in atmospheres of 10:1 (red) and 30:1 (blue) H_2:H_2O

To compare NCF and NCFCo, thin film electrodes were measured in an atmosphere of 10:1 H_2:H_2O obtaining the I-V curves shown in Fig. 4.16. The electrochemical switching point of the two electrodes occurred at different overpotentials as the vertical line marks the electrochemical switching point of Fe. Moreover, after applying a certian cathodic polarisation, the curve of NCFCo seems to split into two partly overlapping discontinuities. Indeed under these conditions (atmosphere = 10:1 (H_2:H_2O), max. cathodic bias = −450 °C), however, Fe^0 should already show exsolutions, considering previous experiments under similar conditions. Therefore

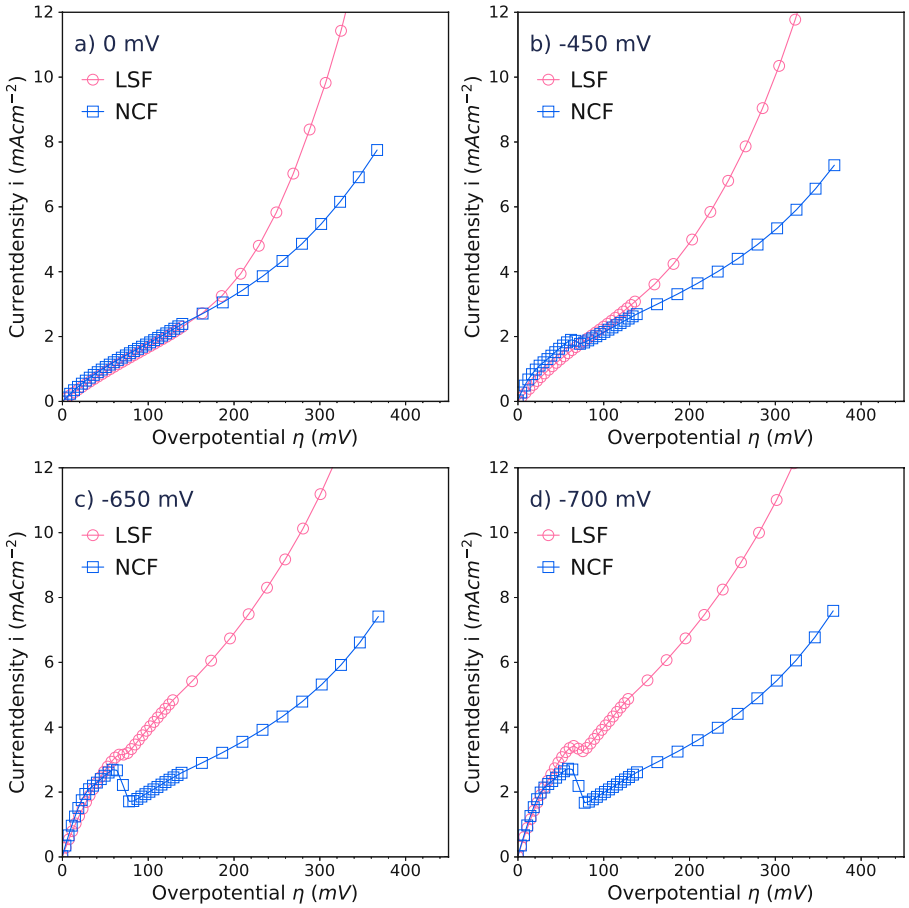

Figure 4.14: I-V curves of samples with either a LSF (red) or an NCF (blue) thin film electrode recorded in an atmosphere of 10:1 H_2:H_2O with an onset hold time of 1 min

it can be assumed that the exsolutions of Co^0 and Fe^0 would lead to a different electrochemical switching behaviour compared to the electrochemical switching point of a singular species. However, despite the modified shaped of the curve, the switching point of Fe^0 is not clearly visible and seem to be shifted to a higher overpotential. Further details on the details on the behaviour of these bimetallic exsolutions, though being very interesting, would go beyond the scope of this thesis.

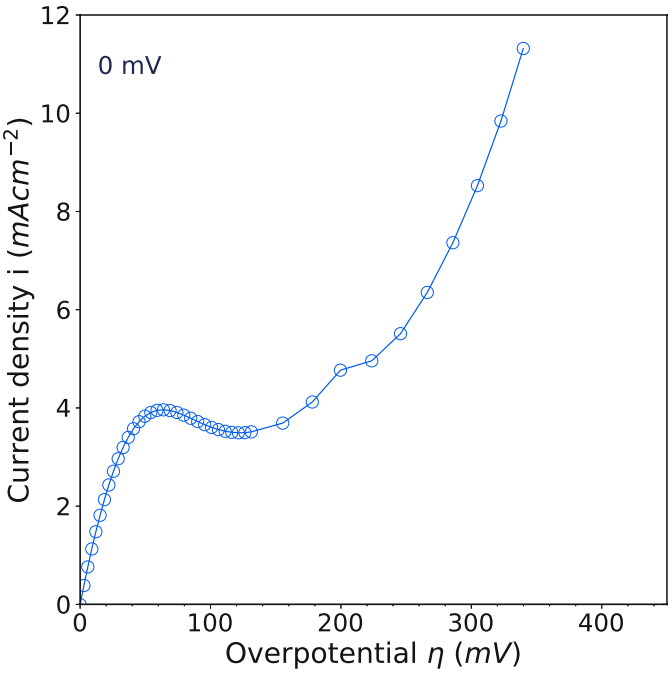

Figure 4.15: I-V curve of a sample with a NCFCo thin film electrode recorded in an atmosphere of 1:1 H_2:H_2O with an onset hold time of 1 min

In Fig. 4.17 the onset potential is summarized for the different thin film electrodes. Samples with LSF thin film electrodes are illustrated in red and those with NCF in blue. Hatched bars describe measurement series with an onset hold time of 60 min and bare ones those with an onset hold time of 1 min.

It can be seen that NCF thin film electrodes under an atmosphere of 30:1 measured with an onset hold time of 60 min required the least cathodic polarisation to perform exsolution, i.e. have the lowest onset potential. On the contrary, LSF in an atmosphere of 10:1 with a onset hold time of 1 min required the highest cathodic polarisation to perform exsolutions. In general, NCF samples showed a lower onset potential than LSF samples and more reductive atmospheres and longer duration of the cathodic bias showed a positive influence on the exsolution behaviour.

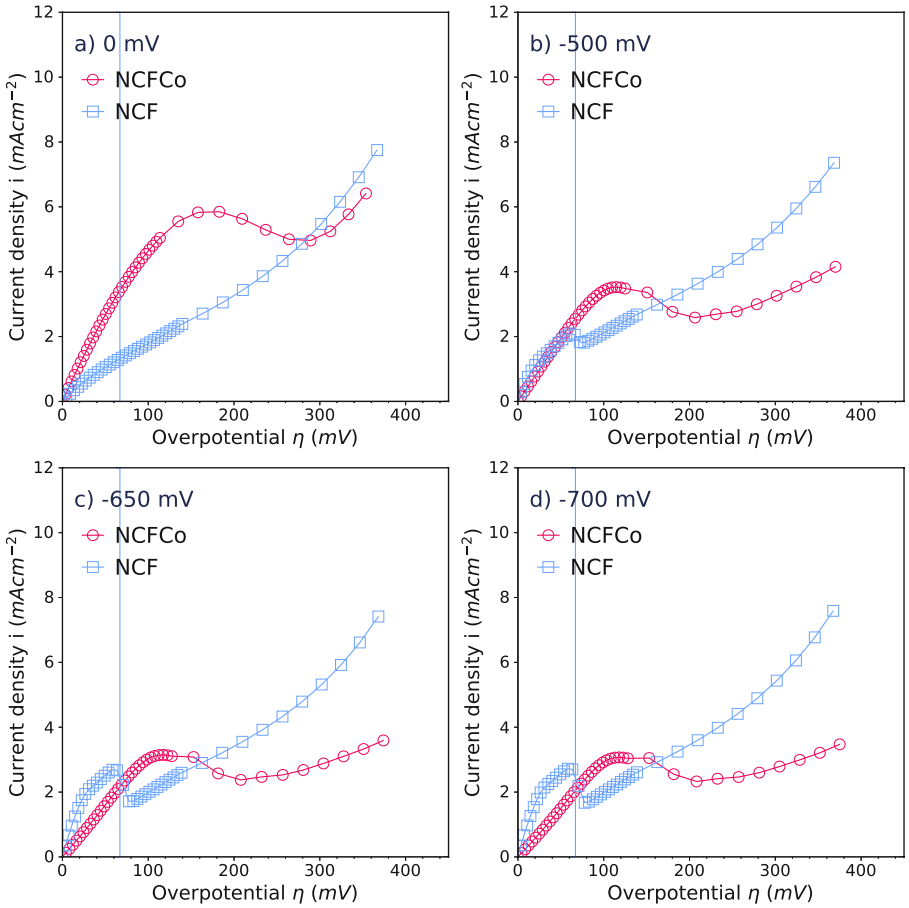

Figure 4.16: I-V curves of NCFCo and NCF thin film electrodes in an atmosphere of 10:1 H_2:H_2O with an onset hold time of 1 min the vertical line marks the electrochemical switching point of Fe

4.2.4 Relation between Oxygen Partial Pressure and Overpotential Required for the Electrochemical Switching

The goal of the following experiments was to get a more detailed insight into the relation between overpotential and oxygen partial pressure. The corresponding measurement program was already described in Subsec. 2.5.2. In the first measure-

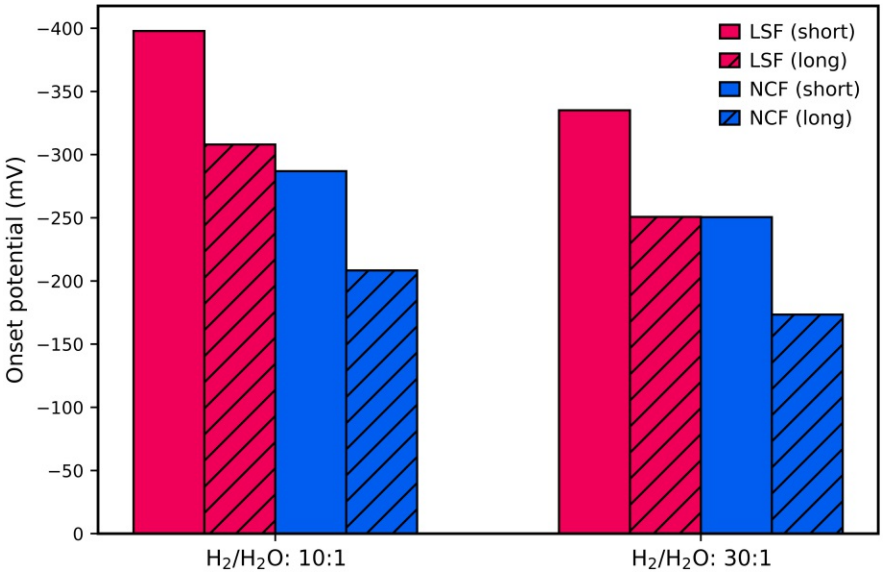

Figure 4.17: Onset potential dependence of to atmosphere and duration (60 min striped, 1 min of the applied cathodic bias illustrated via a bar plot, where samples with LSF thin film electrodes (red) and NCF electrodes (blue) are compared

ment series, the H_2 content was increased, and thus the oxygen partial pressure of the gas mixture was decreased. One measurement series consisted of 13 I-V curves, and due to the pyramid style of the method, every atmosphere was measured twice except for 100:1 H_2:H_2O. "Up" describes I-V curves measured towards 100:1 H_2:H_2O and "Down" describes I-V curves back to the atmosphere of 1:1 H_2:H_2O. This measurement series were conducted after DC measurements in constant atmospheres, where the onset potential was analysed and the electrode surface thus already contain exsolved Fe particles.

In addition a second kind of measurement series that varied in atmosphere ratio was established. This method is very similar to the one mention mentioned above. The only difference was that the ratio of H_2:H_2O varied from 1:1 to 1:100 (i.e. to more oxidising conditions) with the same step size as the method above. In this

atmosphere, the electrochemical switching point is shifted to the cathodic part of the I-V curve and thus no longer leads to a discontinuity in the function, which means that the exsolution behaviour could no longer be seen as a discontinuity in the I-V curve. Three resulting I-V curves of such a measurement are shown in Fig. 4.18. The vertical lines mark the thermodynamic switching point of Fe at the given conditions.

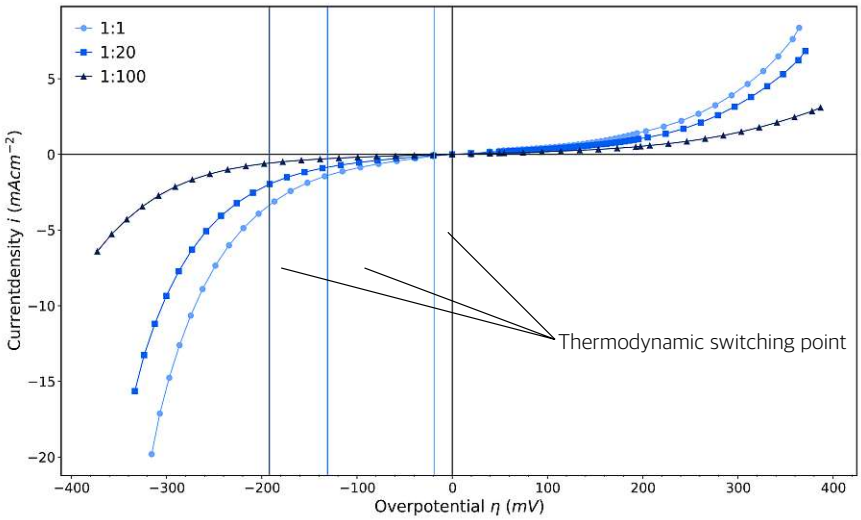

Figure 4.18: Three I-V curves of a measurement series with decreasing H_2 content of a LSF thin film electrode in an atmosphere of 1:1, 1:20 and 1:100 H_2:H_2O and their thermodynamic switching points

Analysis of A-Site Doped Perovskite

In order to analyse the correlation of the corresponding overpotential of the electrochemical switching point and the oxygen partial pressure, DC measurements with varying atmospheres were conducted on samples with LSF and NCF thin film

electrodes. In Fig. 4.19 an exemplary set of DC measurements is shown. For this measurements a bias rang from 400 mV to −400 mV was chosen and the sample has already been measured in onset DC measurement series. It is noticeable that the ”Up” I-V curves (i.e. form moderate to strongly reducing conditions purple) showed exsolution at first in an atmosphere of 60:1 H_2:H_2O. In contrast, the I-V curves of the ”Down” measurement series (i.e. form strongly reducing to moderate reducing conditions blue) showed the electrochemical switching point still under an atmosphere of 10:1 H_2:H_2O. This effect may be explained by the assumption that the particles on the surface formed by initial onset experiment got deactivated and -given that they were sufficient small, thus only containing small amounts of iron- diffused back into the host lattice during the EIS measurements in an atmosphere of 1:1 H_2:H_2O before the DC measurement series. Therefore, Fe needs to exsolve again to show the electrochemical switching point. When the sample showed exsolution during the DC measurement series with varied atmospheres, it seems that the particles sustained on the surface, so the electrochemical switching point remained in more oxidising atmospheres. This behaviour indicates that the amount of Fe on the electrode surface after exsolution onset experiment was small enough, and the time needed for the AC measurements in more oxidising conditions was long enough to redissolve Fe in the perovskite host lattice and thus be reverse the exsolution processes completely.

An excerpt of a DC measurement series in varying atmospheres for a sample with NCF thin film electrodes is shown in Fig. 4.20. The electrochemical switching point started to appear at an atmosphere of 80:1 H_2:H_2O and got clear visible at the I-V

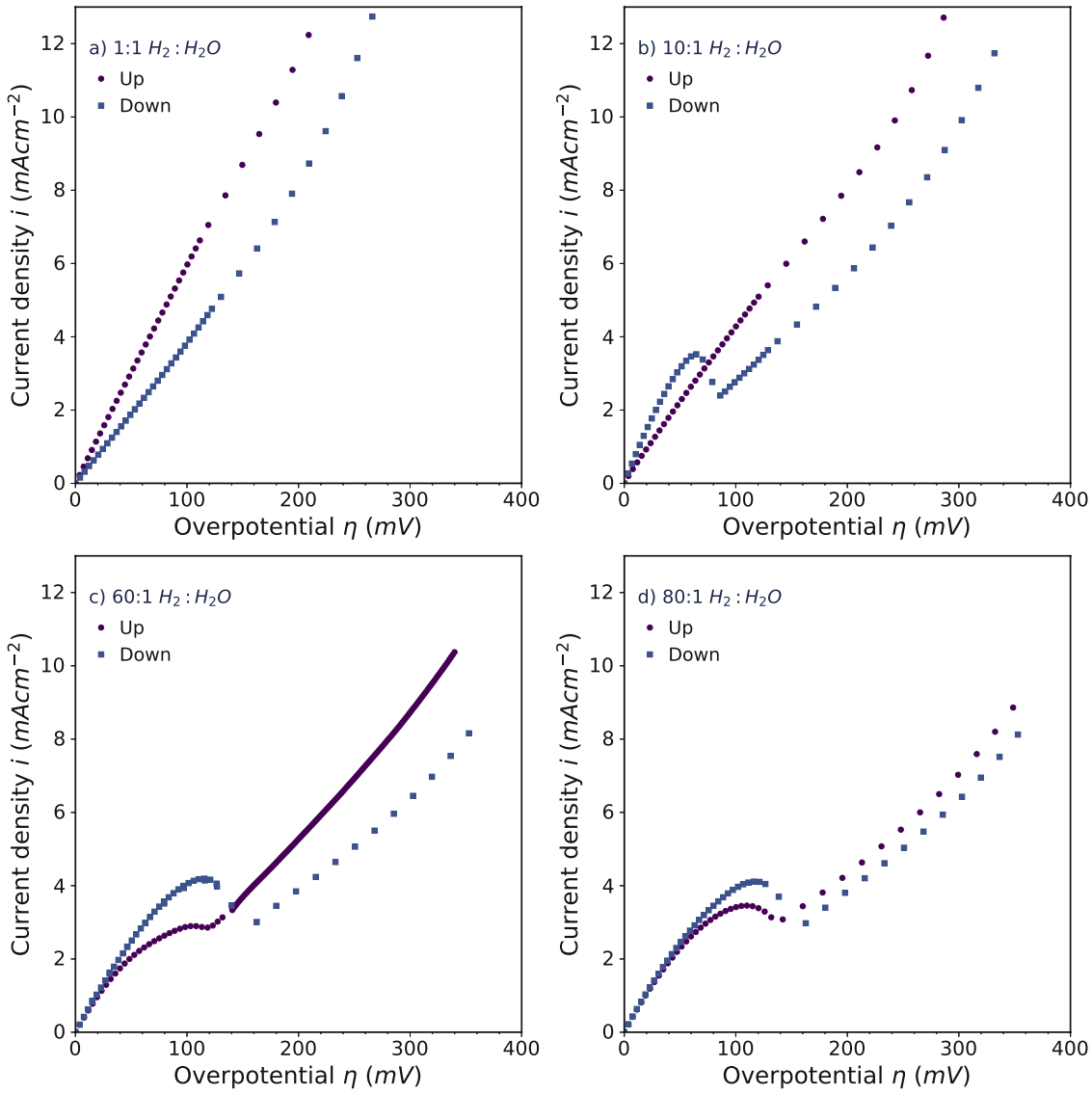

Figure 4.19: Selected I-V curves of a sample with LSF thin film electrode recorded with a DC measurement in varying atmospheres (1:1, 10:1, 60:1 and 100:1)

curves of the ”Down” measurements and can be observed down to an atmosphere of 10:1 H_2:H_2O. Therefore, it can be said that the NCF thin-film electrode behaves very similar to the LSF thin film electrodes, and the behaviour can be explained

analogously. Due to the position of the thermodynamic switching point (−19 mV) in both cases the absence of the electrochemical switching point in an atmosphere of 1:1 H_2:H_2O is as expected.

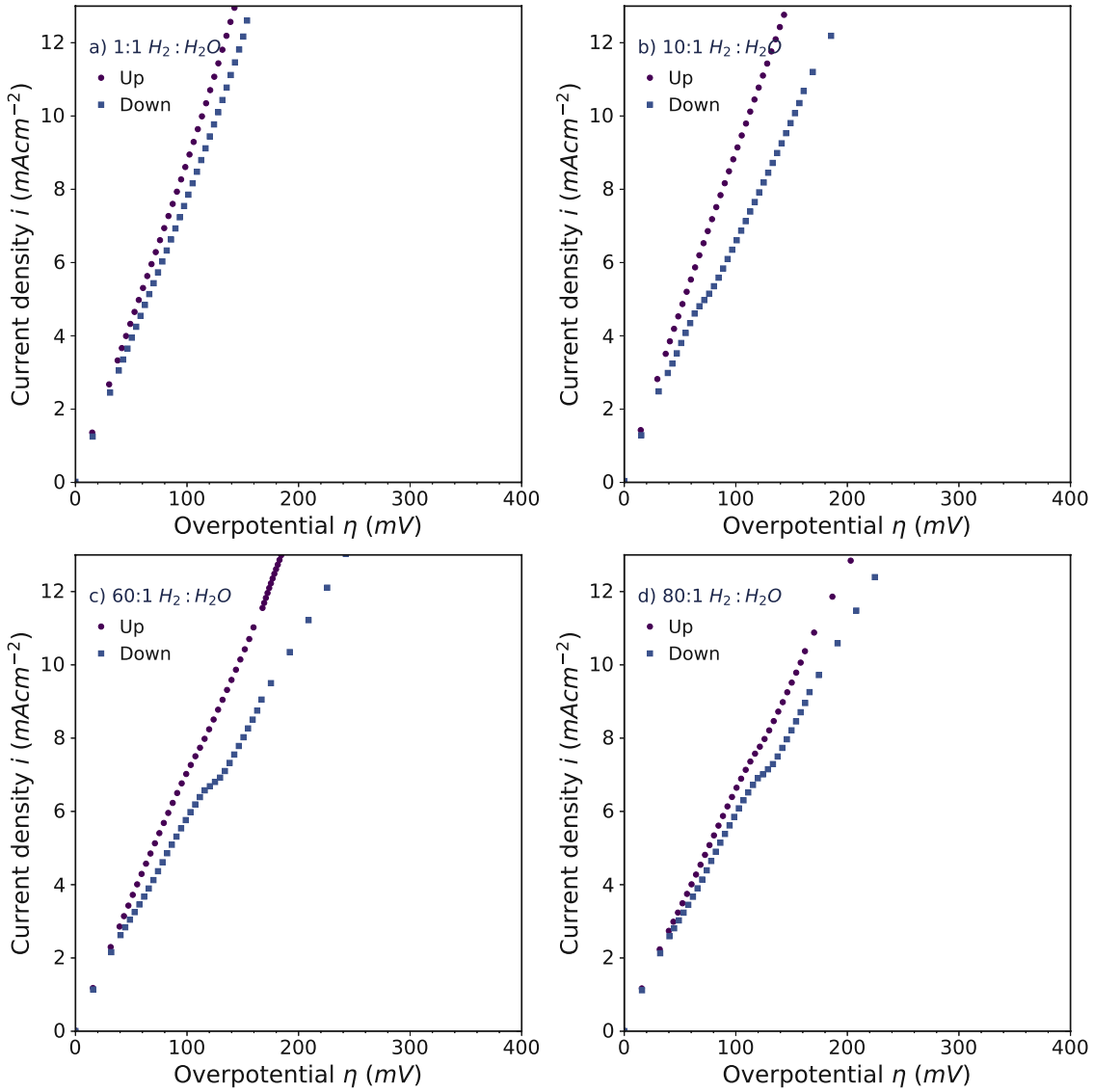

Figure 4.20: I-V selected curves of an sample with an NCF thin film electrode recorded with a DC measurement in varying atmospheres (1:1, 10:1, 60:1 and 100:1)

Fig. 4.20 and Fig. 4.19 clearly show that with increasing H_2 content in the atmosphere, also the overpotential, necessary for the electrochemical switching point increased. This conforms the trend already shown in Fig. 4.12. A shift of the electrochemical switching points was noticed, when the I-V curves of different atmospheres with similar working electrodes and onset hold times are compared. To illustrate this behaviour, two I-V curves of a sample with LSF thin film electrodes are shown in Fig. 4.21. I-V curves measured in atmospheres of 20:1 and 100:1 H_2:H_2O were chosen as example for this comparison. As already mentioned in Subsec. 4.2.3 this effect is caused by the fact that an overpotential shifts the oxygen chemical potential in the electrode and thus anodic polarisation can compensate for the more reducing atmosphere.

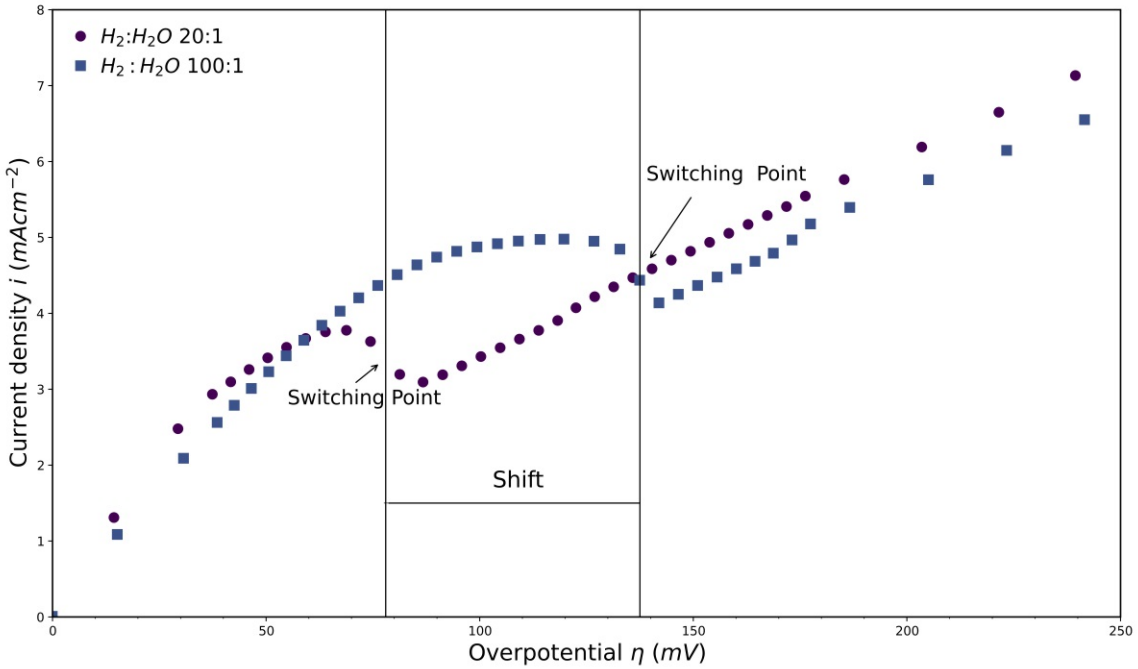

Figure 4.21: I-V curves of a sample with LSF thin film electrodes recorded with a DC measurement in varied atmospheres (20:1 (purple) and 100:1 (blue) H_2:H_2O)

To create a relation between overpotential and oxygen partial pressure, an equivalent oxygen partial pressure for the corresponding atmosphere ratio of H_2:H_2O was calculated. To determine the Gibb's standard Energy for the hydrogen/water equilibrium shown in Eq. (4.2) the standard reaction enthalpy ($\Delta_R H^0$) is required, which can be obtained inserting the enthalpy values of the reactants and products ($H^0_{O_2} = 18.32\,\mathrm{kJ\,mol^{-1}}$, $H^0_{H_2} = 16.87\,\mathrm{kJ\,mol^{-1}}$, $H^0_{H_2O} = -220.96\,\mathrm{kJ\,mol^{-1}}$) in the Hess theorem Eq. (4.3). The standard entropy of the reaction ($\Delta_R S^0 = -108.68\,\mathrm{J\,kmol^{-1}}$) was calculate by inserting the values of the single entropies ($S^0_{O_2} = 238.89\,\mathrm{J\,kmol^{-1}}$, $S^0_{H_2} = 162.15\,\mathrm{J\,kmol^{-1}}$, $S^0_{H_2O} = 227.25\,\mathrm{J\,kmol^{-1}}$) in Eq. (4.4). The values for the enthalpy and entropy are taken from a thermodynamic database [54].

$$2\,H_2 + O_2 \longrightarrow 2\,H_2O \tag{4.2}$$

$$\Delta_R H^0 = 2\,H^0_{H2O} - 2\,H^0_{H2} - H^0_{O2} \tag{4.3}$$

$$\Delta_R S^0 = 2\,S^0_{H2O} - 2\,S^0_{H2} - S^0_{O2} \tag{4.4}$$

The calculated $\Delta_R H^0$ and $\Delta_R S^0$ were used to determine $\Delta_R G^0$ (= −399.09 kJ mol^{-1}) by using Eq. (4.5) where T denotes the temperature (T = 600 °C = 873.15 K).

$$\Delta_R G^0 = \Delta_R H^0 - \Delta_R S^0 T \tag{4.5}$$

In the next step $\Delta_R G^0$ was inserted in Eq. (4.6), where T denotes the temperature and R the ideal gas constant (R = 8.3145 J kmol^{-1}) and so a value for the mass action constant K_a was obtained.

$$K_a = e^{-\frac{\Delta_R G^0}{RT}} \tag{4.6}$$

By multiplying K_a by the standard pressure (p^0 = 1.013 25 *bar*), according to Eq. (4.7), where n denotes the stoichiometry factors of Eq. (4.2), where the signs of the reagents are negative, and the signs of the products are positive, the pressure-dependent equilibrium constant K_p was obtained.

$$K_p = K_a p^{0 \sum n} \tag{4.7}$$

In the last step, by using K_p, an oxygen partial pressure for the responding atmospheres can be calculated, as shown in Eq. (4.8), where $\frac{H_2}{H_2O}$ gives the ratio of hydrogen to water.

$$p_{O_2} = (\frac{H_2}{H_2O})^2 K_p \tag{4.8}$$

In order to visualise the relation between the overpotential required to electrochemically switching Fe^0 into Fe-oxide and the surrounding oxygen partial pressure, the measured electrochemical switching points and the calculated thermodynamic switching point were plotted versus the equivalent oxygen partial pressure in the electrode, shown in Fig. 4.22. This plot contains data from three LSF samples, which were fitted with a exponential regression, and the resulting regression line is shown by the dark blue line. Moreover, the plot also contains the thermodynamic switching point shown by the light blue line. As can be seen, the line of the obtained electrochemical switching point lies above the linear of the thermodynamic data. This gap was defined as $\Delta\eta_{sw}$, which stands for the additional overpotential that was necessary to perform oxidation of exsolved Fe^0 particles on the electrode surface. Interestingly, at lower $p(O_2)$ the measured values are closer to the thermodynamic data as this is not the case for higher $p(O_2)$, which is quit unexpected behaviour and point towards a measurement artifice. A possible reason could be a limitation of the accuracy of the mass flow control system at higher p_{H_2} pressure.

Alternatively, a carry-over for water from more p(H_2O) rich conditions to the atmospheres with very low p(H_2O) may have occurred, due to its strong adsorptive tendency.

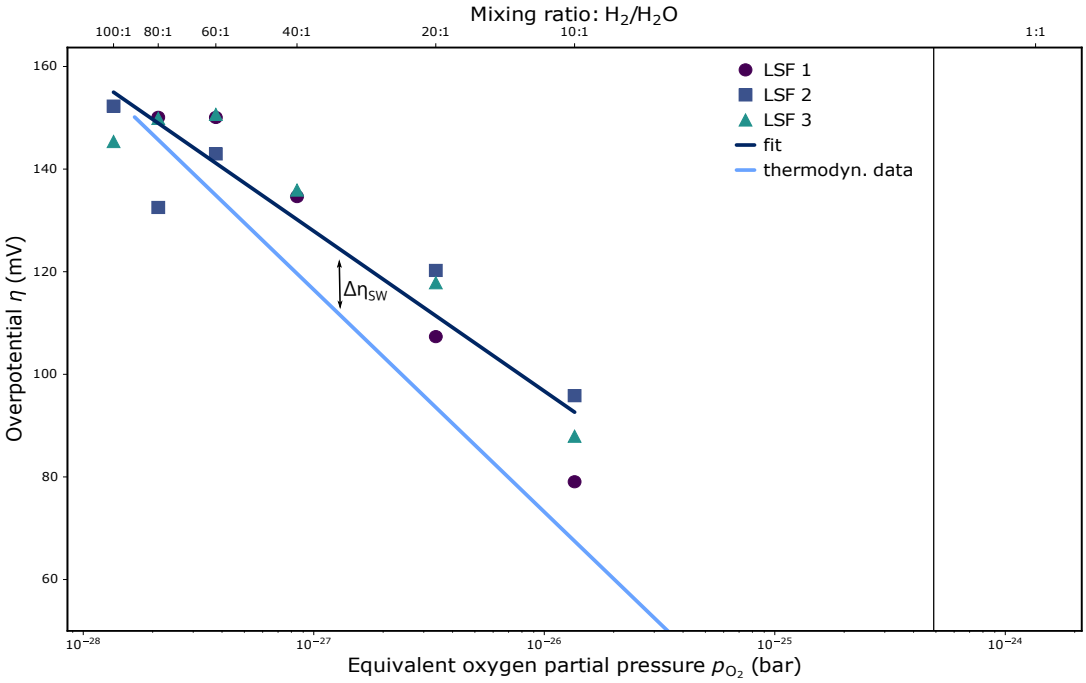

Figure 4.22: Linear regression of three different LSF samples of the overpotential of their electrochemical switching point at the atmospheres DC measurement series with varied atmospheres and the equivalent oxygen partial pressure and the linear of the thermodynamic data of the reduction and oxidation of Fe^0 and the resulting $\Delta\eta_{sw}$

Analysis of A- and B-Site Doped Perovskite

In this part of the experiments, DC measurement series with varying atmospheres were conducted on A- and B-site doped perovskite. NCFCo was used as a thin-film electrode. Fig. 4.23 shows the measured I-V curves starting from an atmosphere

of 1:1 H_2:H_2O (”Up” and ”Down”). Due to the previous experiments with one-site doped perovskites, it can be assumed that Co alone exsolved . Taking the course of the measurement series into account, it can be seen that on the way up the electrochemical switching point change after its appearance after a DC measurement in an atmosphere of 60:1 H_2:H_2O. A likely explanation for this could be that Fe started to perform exsolution at this point, and the presence of both catalytic species changed the appearance of the electrochemical switching point. It is worth noticing that all recorded I-V curves on the way back to an atmosphere of 1:1 H_2:H_2O kept this appearance even during the last measurement. This could be caused by the mixture of Co and Fe on the sample surface, which both remained present on the surface in the more oxidising condition. However, it is worth emphasising, that from electrochemical experiments alone the chemical state of the exsolution can not be conducted unambiguously. To clarify this question, X-ray photoelectron spectroscopy measurements will be required in the future.

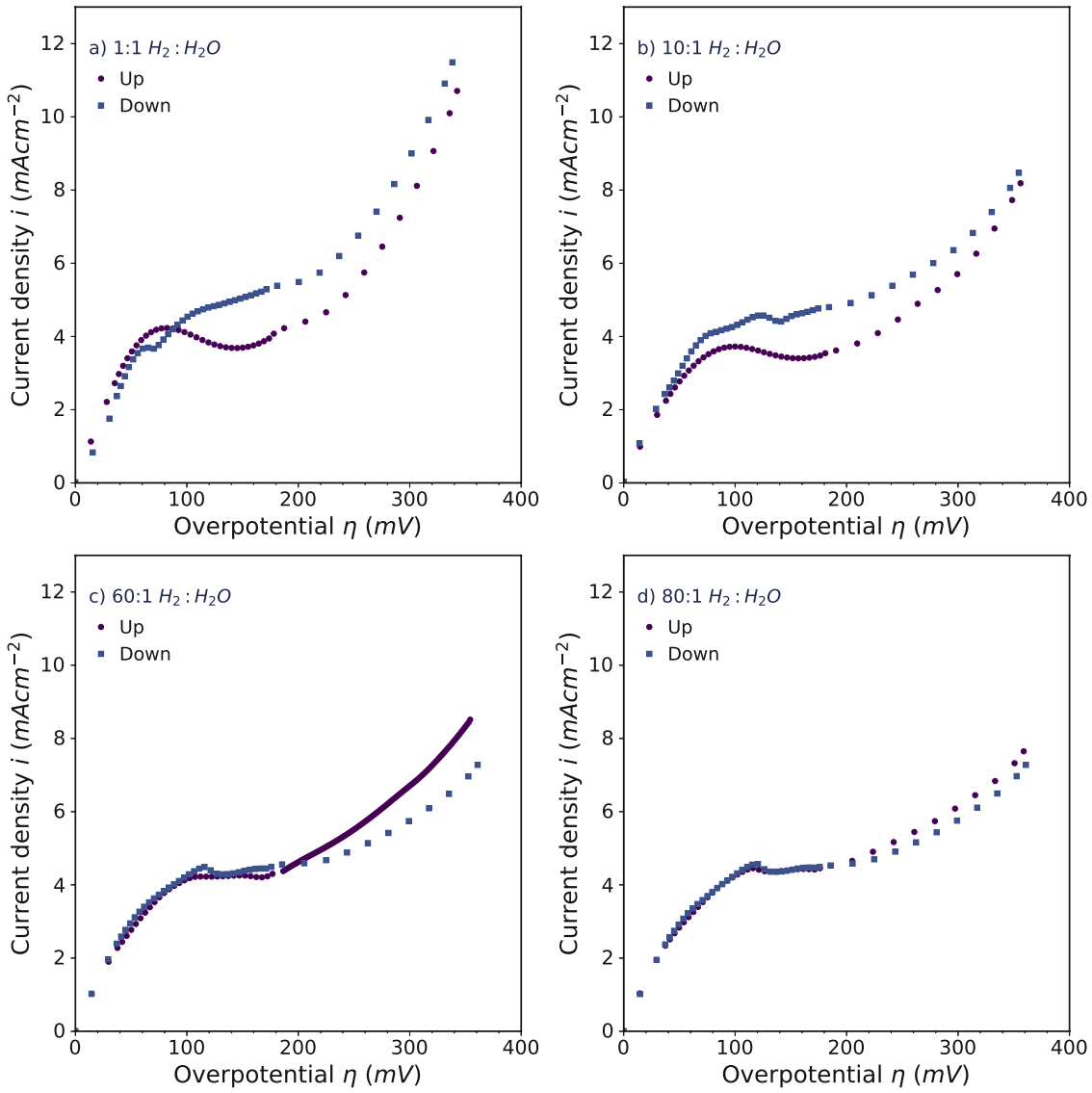

Figure 4.23: I-V cures of NCFCo thin-film electrodes measured with a DC measurement series in atmospheres of 1:1, 10:1, 60:1 and 100:1

5 Conclusion

This work studies the exsolution behaviour of different transition metals (Fe and Co) from perovskite-type, thin film electrodes as well as the electrochemical switching behaviour of the catalytic activity of the obtained surface particles.

Novel results were obtained in terms of:

- The onset potential of different thin film electrodes in varying reaction conditions in regard to a different polarisation time, different electrode materials and a varying H_2 to H_2O ratio
- The electrochemical switching behaviour of multiple thin film electrodes relating to varying compositions, $Nd_{0.6}Ca_{0.4}FeO_{3-\delta}$ (NCF), $La_{0.6}Sr_{0.4}FeO_{3-\delta}$(LSF), $Nd_{0.6}Ca_{0.4}Fe_{0.9}Co_{0.1}O_{3-\delta}$(NCFCo))
- The interplay of oxygen partial pressure and overpotential during electrochemical switching including a quantitative comparison with the expected thermodynamic behaviour

To achieve these results, electrochemical impedance spectroscopy and DC current voltage characteristics served as the main analysis tool. The aim of the impedance experiments was to determine the offset resistance (R_{YSZ}) of the studied model cells in order to calculate the overpotential for the I-V curves correctly and to get an impression of the electro-catalytic activity of the sample. For example, it was observed that after exsolution had been performed the sample showed a lower working electrode resistance for LSF and NCF. For NCFCo samples it was not possible to measure EIS spectra before exsolution, since Co was already exsolved under the given atmosphere conditions. Never the less, indications of an increase in resistance of the working electrode were found, when Fe was also present on the surface.

Additionally, it was observed how to trigger exsolutions by applying a cathodic bias and subsequently monitoring the exsolution behaviour via the appearance of a characteristic feature in the anodic part of the I-V curve. Based on the results of the DC experiments, it was concluded that the onset potential of different perovskite thin film electrodes strongly depends on the reaction conditions, compounded through varying the electrode materials, onset holding times of the cathodic bias and the atmosphere. It was observed, that the onset point is lower at a longer onset hold time of the cathodic bias for initial exsolutions and in more reducing atmospheres. Furthermore, it was demonstrated that, unlike NCE, LSF needs more cathodic bias in order to present a first appearance of exsolutions. Consequently, it was concluded that, the exsolution onset depends on the material of the electrode, i.e. the perovskite-typ host oxide.

The catalytic activity of particles on the electrode surface were studied by analyses of the initial exsolution point and the reaction conditions, which influence the electrochemical switching of the respectively species. Through out the experiments the notion that electrochemical switching behaviour is disassociated from the onset hold time cloud be underlined. In addition, it was observed that the exsolution onset for single species, e.g. Fe, appears independent from the perovskite-type host martial of the thin film electrode, as demonstrated by experiments with LSF and NCF.

The last part of this thesis focuses on a correlation between the overpotential needed to switch catalytically active Fe^0 particles into less active Fe-oxides and the oxygen partial pressure in the atmosphere. The possible existence of a clear Nernst-like correlation of the electrochemical switching point with the equivalent $p(O_2)$ was demonstrated. In continuation, the actually observed switching point bias was at a slightly more anodic potential than expected off of thermodynamic considerations, therefore a kinetic part of the reaction can be assumed.This experiment indicates that the switching process itself (i.e. the transition between Fe and Fe-oxide particles on the surface) is a competitive process between the conducting electrode driving towards oxidation and the reducing potential of the atmosphere.

Considering the DC measurement series in varying atmospheres, it can be assumed that small amounts of Fe are able to incorporate back in the perovskite lattice at atmospheres of 1:1 H_2:H_2O, due to the fact that the first ”Up” I-V curves did not show any electrochemical switching behaviour. Depending on the sample, the first signs of exsolutions appeared in atmospheres between 60:1 and 80:1 H_2:H_2O.

However, the I-V curves of the ”down” measurements kept their electrochemical switching point. This behaviour was also observed during analysing Fe on the surfaces of NCFCo electrodes.

It was furthermore shown that when utilising double doped perovskites as NCFCo the presence of Fe and Co particles on the electrode's surface affected the electrochemical switching point of both elements. However, Fe seems to have a similar onset bias in NCF and NCFCo, meaning that the onset potential was not impacted by doping the material. Considering the second measurement series conducted under varying atmospheres, it can be assumed that the change in appearance of the electrochemical switching point is reversible, as the I-V curve only showed the switching point for Co during the first ”Up” curves when persuadable no more Fe remained at the surface.

Bibliography

[1] EU. *The Commission calls for a climate neutral Europe by 2050*. 2019. URL: https://ec.europa.eu/commission/presscorner/detail/en/IP_18_6543.

[2] E. COMMISSION. *The Paris Protocol A blueprint for tackling global climate change beyond 2020*. 2015. URL: https://ec.europa.eu/clima/sites/default/files/international/paris_protocol/docs/com_2015_81_en.pdf.

[3] statista. *CO2-Emissionen weltweit in den Jahren 1960 bis 2019*. Ed. by statista. 2020. URL: https://de.statista.com/statistik/daten/studie/37187/umfrage/der-weltweite-co2-ausstoss-seit-1751/.

[4] EU. *EU climate action and the European Green Deal*. 2021. URL: https://ec.europa.eu/clima/policies/eu-climate-action_en.

[5] B. Timurkutluk, C. Timurkutluk, M. D. Mat, and Y. Kaplan. "A review on cell stack designs for high performance solid oxide fuel cells". In: *Renewable and Sustainable Energy Reviews* 56 (Apr. 2016), pp. 1101–1121. DOI: 10.1016/j.rser.2015.12.034.

[6] Z. Shao and S. M. Haile. "A High-Performance Cathode for the Next Generation of Solid-Oxide Fuel Cells." In: *ChemInform* 35.47 (Nov. 2004). DOI: 10.1002/chin.200447014.

[7] N. Sammes, ed. *Fuel Cell Technology*. Springer London, 2006. DOI: 10.1007/1-84628-207-1.

[8] X. Yu and S. Ye. "Recent advances in activity and durability enhancement of Pt/C catalytic cathode in PEMFC". In: *Journal of Power Sources* 172.1 (Oct. 2007), pp. 145–154. DOI: 10.1016/j.jpowsour.2007.07.048.

[9] S. Gamburzev and A. Appleby. "Recent progress in performance improvement of the proton exchange membrane fuel cell (PEMFC)". In: *Journal of Power Sources* 107.1 (Apr. 2002), pp. 5–12. DOI: 10.1016/s0378-7753(01)00970-3.

[10] O. Ijaodola, Z. E. Hassan, E. Ogungbemi, F. Khatib, T. Wilberforce, J. Thompson, and A. Olabi. "Energy efficiency improvements by investigating the water flooding management on proton exchange membrane fuel cell (PEMFC)". In: *Energy* 179 (July 2019), pp. 246–267. DOI: 10.1016/j.energy.2019.04.074.

[11] P. J. Hamilton and B. G. Pollet. "Polymer Electrolyte Membrane Fuel Cell (PEMFC) Flow Field Plate: Design, Materials and Characterisation". In: *Fuel Cells* 10.4 (May 2010), pp. 489–509. DOI: 10.1002/fuce.201000033.

[12] X.-M. Ge, S.-H. Chan, Q.-L. Liu, and Q. Sun. "Solid Oxide Fuel Cell Anode Materials for Direct Hydrocarbon Utilization". In: *Advanced Energy Materials* 2.10 (Aug. 2012), pp. 1156–1181. DOI: 10.1002/aenm.201200342.

[13] S. Singhal. "Advances in solid oxide fuel cell technology". In: *Solid State Ionics* 135.1-4 (Nov. 2000), pp. 305–313. DOI: 10.1016/s0167-2738(00)00452-5.

[14] M. Laguna-Bercero. "Recent advances in high temperature electrolysis using solid oxide fuel cells: A review". In: *Journal of Power Sources* 203 (Apr. 2012), pp. 4–16. DOI: 10.1016/j.jpowsour.2011.12.019.

[15] A. Stambouli and E. Traversa. "Solid oxide fuel cells (SOFCs): a review of an environmentally clean and efficient source of energy". In: *Renewable and Sustainable Energy Reviews* 6.5 (Oct. 2002), pp. 433–455. DOI: 10.1016/s1364-0321(02)00014-x.

[16] N. Q. Minh. "Ceramic Fuel Cells". In: *Journal of the American Ceramic Society* 76.3 (Mar. 1993), pp. 563–588. DOI: 10.1111/j.1151-2916.1993.tb03645.x.

[17] M. Pihlatie, T. Ramos, and A. Kaiser. "Testing and improving the redox stability of Ni-based solid oxide fuel cells". In: *Journal of Power Sources* 193.1 (Aug. 2009), pp. 322–330. DOI: 10.1016/j.jpowsour.2008.11.140.

[18] M. Gong, X. Liu, J. Trembly, and C. Johnson. "Sulfur-tolerant anode materials for solid oxide fuel cell application". In: *Journal of Power Sources* 168.2 (June 2007), pp. 289–298. DOI: 10.1016/j.jpowsour.2007.03.026.

[19] S. McIntosh and R. J. Gorte. "Direct Hydrocarbon Solid Oxide Fuel Cells". In: *Chemical Reviews* 104.10 (Oct. 2004), pp. 4845–4866. DOI: 10.1021/cr020725g.

[20] M. D. Gross, J. M. Vohs, and R. J. Gorte. "Recent progress in SOFC anodes for direct utilization of hydrocarbons". In: *Journal of Materials Chemistry* 17.30 (2007), p. 3071. DOI: 10.1039/b702633a.

[21] G. Kim, S. Lee, J. Y. Shin, G. Corre, J. T. S. Irvine, J. M. Vohs, and R. J. Gorte. "Investigation of the Structural and Catalytic Requirements for High-Performance SOFC Anodes Formed by Infiltration of LSCM". In: *Electrochemical and Solid-State Letters* 12.3 (2009), B48. DOI: 10.1149/1.3065971.

[22] D. Simwonis. "Nickel coarsening in annealed Ni/8YSZ anode substrates for solid oxide fuel cells". In: *Solid State Ionics* (2000).

[23] Y. Nishihata, J. Mizuki, T. Akao, H. Tanaka, M. Uenishi, M. Kimura, T. Okamoto, and N. Hamada. "Self-regeneration of a Pd-perovskite catalyst for automotive emissions control". In: *Nature* 418.6894 (July 2002), pp. 164–167. DOI: 10.1038/nature00893.

[24] H. Tanaka, M. Taniguchi, M. Uenishi, N. Kajita, I. Tan, Y. Nishihata, J. Mizuki, K. Narita, M. Kimura, and K. Kaneko. "Self-Regenerating Rh- and Pt-Based Perovskite Catalysts for Automotive-Emissions Control". In: *Angewandte Chemie* 118.36 (Sept. 2006), pp. 6144–6148. DOI: 10.1002/ange.200503938.

[25] L. Adijanto, V. B. Padmanabhan, R. J. Gorte, and J. M. Vohs. "Polarization-Induced Hysteresis in CuCo-Doped Rare Earth Vanadates SOFC Anodes". In: *Journal of The Electrochemical Society* 159.11 (2012), F751–F756. DOI: 10.1149/2.042211jes.

[26] S. Sengodan, Y.-W. Ju, O. Kwon, A. Jun, H. Y. Jeong, T. Ishihara, J. Shin, and G. Kim. "Self-Decorated MnO Nanoparticles on Double Perovskite Solid Oxide Fuel Cell Anode by in Situ Exsolution". In: *ACS Sustainable Chemistry & Engineering* 5.10 (Sept. 2017), pp. 9207–9213. DOI: 10.1021/acssuschemeng.7b02156.

[27] Y.-F. Sun, Y.-Q. Zhang, J. Chen, J.-H. Li, Y.-T. Zhu, Y.-M. Zeng, B. S. Amirkhiz, J. Li, B. Hua, and J.-L. Luo. "New Opportunity for in Situ Exsolution of Metallic Nanoparticles on Perovskite Parent". In: *Nano Letters* 16.8 (July 2016), pp. 5303–5309. DOI: 10.1021/acs.nanolett.6b02757.

[28] T. Cao, O. Kwon, R. J. Gorte, and J. M. Vohs. "Metal Exsolution to Enhance the Catalytic Activity of Electrodes in Solid Oxide Fuel Cells". In: *Nanomaterials* 10.12 (Dec. 2020), p. 2445. DOI: 10.3390/nano10122445.

[29] M. Andersson, H. Paradis, J. Yuan, and B. Sundén. "Review of catalyst materials and catalytic steam reforming reactions in SOFC anodes". In: *International Journal of Energy Research* 35.15 (June 2011), pp. 1340–1350. DOI: 10.1002/er.1875.

[30] C. Ni, Q. Zeng, D. He, L. Peng, D. Xie, J. T. S. Irvine, S. Duan, and J. Ni. "A B-site doped perovskite ferrate as an efficient anode of a solid oxide fuel cell with in situ metal exsolution". In: *Journal of Materials Chemistry A* 7.47 (2019), pp. 26944–26953. DOI: 10.1039/c9ta09916f.

[31] T. Zhu, H. E. Troiani, L. V. Mogni, M. Han, and S. A. Barnett. "Ni-Substituted Sr(Ti,Fe)O3 SOFC Anodes: Achieving High Performance via Metal Alloy Nanoparticle Exsolution". In: *Joule* 2.3 (Mar. 2018), pp. 478–496. DOI: 10.1016/j.joule.2018.02.006.

[32] D. Neagu, G. Tsekouras, D. N. Miller, H. Ménard, and J. T. S. Irvine. "In situ growth of nanoparticles through control of non-stoichiometry". In: *Nature Chemistry* 5.11 (Oct. 2013), pp. 916–923. DOI: 10.1038/nchem.1773.

[33] G. Tsekouras, D. Neagu, and J. T. S. Irvine. "Step-change in high temperature steam electrolysis performance of perovskite oxide cathodes with exsolution of B-site dopants". In: *Energy Environ. Sci.* 6.1 (2013), pp. 256–266. DOI: 10.1039/c2ee22547f.

[34] A. K. Opitz, A. Nenning, C. Rameshan, R. Rameshan, R. Blume, M. Hävecker, A. Knop-Gericke, G. Rupprechter, J. Fleig, and B. Klötzer. "Enhancing Electrochemical Water-Splitting Kinetics by Polarization-Driven Formation of Near-Surface Iron(0): An In-Situ XPS Study on Perovskite-Type Electrodes". In: *Angewandte Chemie International Edition* 54.9 (Dec. 2014), pp. 2628–2632. DOI: 10.1002/anie.201409527.

[35] A. K. Opitz, A. Nenning, V. Vonk, S. Volkov, F. Bertram, H. Summerer, S. Schwarz, A. Steiger-Thirsfeld, J. Bernardi, A. Stierle, and J. Fleig. "Understanding electrochemical switchability of perovskite-type exsolution catalysts". In: *Nature Communications* 11.1 (Sept. 2020). DOI: 10.1038/s41467-020-18563-w.

[36] C. Hammond. *The Basics of Crystallography and Diffraction*. Oxford University Press, May 2015. DOI: 10.1093/acprof:oso/9780198738671.001.0001.

[37] R. J. Tilley. "Defects in Solids". In: *Encyclopedia of Inorganic and Bioinorganic Chemistry* (2018).

[38] B. Hans-Juergen and S. (Guenter. *Werkstoffkunde*. 2012.

[39] F. Kröger and H. Vink. "Relations between the Concentrations of Imperfections in Crystalline Solids". In: *Solid State Physics*. Elsevier, 1956, pp. 307–435. DOI: 10.1016/s0081-1947(08)60135-6.

[40] M. Kuhn, S. Hashimoto, K. Sato, K. Yashiro, and J. Mizusaki. "Oxygen nonstoichiometry, thermo-chemical stability and lattice expansion of La0.6Sr0.4FeO3-δ". In: *Solid State Ionics* 195.1 (July 2011), pp. 7–15. DOI: 10.1016/j.ssi.2011.05.013.

[41] J. Maier. *Physical Chemistry of Ionic Materials*. John Wiley & Sons, Ltd, Apr. 2004. DOI: 10.1002/0470020229.

[42] T. Sato, S. Takagi, S. Deledda, B. C. Hauback, and S.-i. Orimo. "Extending the applicability of the Goldschmidt tolerance factor to arbitrary ionic compounds". In: *Scientific Reports* 6.1 (Apr. 2016). DOI: 10.1038/srep23592.

[43] A. J. McEvoy. "Materials for high-temperature oxygen reduction in solid oxide fuel cells". In: *Journal of Materials Science* 36.5 (2001), pp. 1087–1091. DOI: 10.1023/a:1004861221167.

[44] J.-H. Myung, D. Neagu, D. N. Miller, and J. T. S. Irvine. "Switching on electrocatalytic activity in solid oxide cells". In: *Nature* 537.7621 (Aug. 2016), pp. 528–531. DOI: 10.1038/nature19090.

[45] L. Lindenthal, R. Rameshan, H. Summerer, T. Ruh, J. Popovic, A. Nenning, S. Löffler, A. K. Opitz, P. Blaha, and C. Rameshan. "Modifying the Surface Structure of Perovskite-Based Catalysts by Nanoparticle Exsolution". In: *Catalysts* 10.3 (Mar. 2020), p. 268. DOI: 10.3390/catal10030268.

[46] J. Fleig. "The grain boundary impedance of random microstructures: numerical simulations and implications for the analysis of experimental data". In: *Solid State Ionics* 150.1-2 (Sept. 2002), pp. 181–193. DOI: 10.1016/s0167-2738(02)00274-6.

[47] Z. Ahmad. "Concrete Corrosion". In: *Principles of Corrosion Engineering and Corrosion Control*. Elsevier, 2006, pp. 609–646. DOI: 10.1016/b978-075065924-6/50013-1.

[48] M. P. Pechini. "Method of preparing lead and alkaline earth titantes and niobates and coating method using the same to form a capacitor". In: (1967).

[49] C. Ahamer, A. K. Opitz, G. M. Rupp, and J. Fleig. "Revisiting the Temperature Dependent Ionic Conductivity of Yttria Stabilized Zirconia (YSZ)". In: *Journal of The Electrochemical Society* 164.7 (2017), F790–F803. DOI: 10.1149/2.0641707jes.

[50] J. Jamnik and J. Maier. "Treatment of the Impedance of Mixed Conductors Equivalent Circuit Model and Explicit Approximate Solutions". In: *Journal of The Electrochemical Society* 146.11 (Nov. 1999), pp. 4183–4188. DOI: 10.1149/1.1392611.

[51] F. Baumann, J. Fleig, H. Habermeier, and J. Maier. "Impedance spectroscopic study on well-defined (La,Sr)(Co,Fe)O3-δ model electrodes". In: *Solid State Ionics* 177.11-12 (Apr. 2006), pp. 1071–1081. DOI: 10.1016/j.ssi.2006.02.045.

[52] F. Juergen, A. Schmid, G. M. Rupp, C. Slouka, E. Navickas, L. Andrejs, H. Hutter, L. Volgger, and A. Nenning. "The Chemical Capacitance as a Fingerprint of Defect Chemistry in Mixed Conducting Oxides". In: *Acta Chimica Slovenica* (Sept. 2016), pp. 509–518. DOI: 10.17344/acsi.2016.2302.

[53] A. Nenning, M. Holzmann, J. Fleig, and A. K. Opitz. "Excellent kinetics of single-phase Gd-doped ceria fuel electrodes in solid oxide cells". In: *In revision* (2021).

[54] D. Siderius. *NIST Standard Reference Simulation Website - SRD 173*. en. 2017. DOI: 10.18434/T4M88Q.